Designing $LiTaO_3:Ln^{3+},Eu^{3+}$ (Ln = Tb or Pr) perovskite dosimeter with excellent charge carrier storage capacity and stability for anti-counterfeiting and flexible X-ray imaging

Lyu, Tianshuai; Dorenbos, Pieter; Wei, Zhanhua

DOI
10.1016/j.cej.2023.141685

Publication date
2023

Document Version
Final published version

Published in
Chemical Engineering Journal

Chemical Engineering Journal 461 (2023) 141685

Contents lists available at ScienceDirect

Chemical Engineering Journal

journal homepage: www.elsevier.com/locate/cej

Designing $LiTaO_3:Ln^{3+},Eu^{3+}$ (Ln = Tb or Pr) perovskite dosimeter with excellent charge carrier storage capacity and stability for anti-counterfeiting and flexible X-ray imaging

Tianshuai Lyu [a,*], Pieter Dorenbos [b], Zhanhua Wei [a,*]

[a] Xiamen Key Laboratory of Optoelectronic Materials and Advanced Manufacturing, Institute of Luminescent Materials and Information Displays, College of Materials Science and Engineering, Huaqiao University, Xiamen 361021, China

[b] Delft University of Technology, Faculty of Applied Sciences, Department of Radiation Science and Technology, Mekelweg 15, 2629JB Delft, the Netherlands

ARTICLE INFO

Keywords:
Eu^{3+} as a good electron trap
VRBE diagram
$LiTaO_3:Ln^{3+},Eu^{3+}$ (Ln=Tb or Pr) perovskite
Designing storage phosphors
Multimode anti-counterfeiting
Flexible X-ray imaging

ABSTRACT

Developing X-ray charged dosimeters with excellent charge carrier storage capacity and stability is challenging. Such energy storage dosimeters have fascinating use in developing novel applications, for instance, in radiation detection, advanced multimode anti-counterfeiting, and flexible X-ray imaging of curved objects. Herein, novel $LiTaO_3:Ln^{3+},Eu^{3+}$ (Ln = Tb or Pr) perovskite dosimeters are reported by combining the vacuum referred binding energy (VRBE) diagram of $LiTaO_3$ and the optimization of dopant's concentration and compound synthesis condition. Based on the VRBE diagram prediction, charge carrier capturing and de-trapping processes in Eu^{3+} and/or Ln^{3+} (Ln = Tb or Pr) doped $LiTaO_3$ will be studied to unravel the role of Eu^{3+} as a good electron trapping centre and to discover a record storage phosphor. The ratios of the thermoluminescence intensity of the optimized $LiTaO_3:0.005Tb^{3+},0.001Eu^{3+}$ to that of the state-of-the-art $BaFBr(I):Eu^{2+}$, $Al_2O_3:C$, or $NaLuF_4:Tb^{3+}$ are 5.2, 8.8, or 2.8, respectively. The charge carriers can be stored more than 1000 h in $LiTaO_3:0.005Tb^{3+},0.001Eu^{3+}$. Proof-of-concept anti-counterfeiting application will be demonstrated by combining the colour-tailorable photoluminescence, afterglow, thermally, or optically stimulated luminescence in $LiTaO_3:0.005Tb^{3+},xEu^{3+}$ and $LiTaO_3:0.005Pr^{3+},0.001Eu^{3+}$. Multimode anti-counterfeiting application will be proposed by combining a high absolute X-ray scintillation light yield of 19000 ± 1800 ph/MeV of $LiTaO_3:0.005Tb^{3+},0.001Eu^{3+}$. Proof-of-concept flexible X-ray imaging application will be demonstrated by using the optimized $LiTaO_3:0.005Tb^{3+}$, $0.001Eu^{3+}$ dispersed in a silicone gel film.

1. Introduction

X-ray flat-panel detector arrays have promising use in various applications, like in X-ray imaging for medical diagnostics [1–3], academic research [4–6], and non-destructive inspection [7–9]. In a general X-ray detector, X-ray energy is measured by the converted charge carriers directly detected by pixelated thin-film phototransistor (TFT) arrays or indirectly detected by a sheet of a scintillator crystal plate, like CsI:Tl, combined with TFT arrays [2,10,11]. Generally, thin-film phototransistors (TFTs) are deposited on an ITO glass substrate. To realize flat-panel X-ray imaging, large area thin-film phototransistor (TFT) arrays are also required to be integrated with a sheet of a scintillator crystal plate [12,13]. Both the thin layer of a scintillator plate and the glass substrate in a TFT array are not bendable. It is then challenging to realize X-ray imaging for curved or irregular objects by using bendable systems [14]. The pixelated thin-film phototransistor arrays and scintillator crystal plate are expensive because of the difficulty in their synthesis and further assembly. There is therefore a demand of new X-ray detectors for irregular objects X-ray imaging [15].

Halide perovskite scintillators [16,17], like $Cs_2AgBiBr_6$ [18], Rb_2CuBr_3 [19], and the $CsPbX_3$ (X = Cl, Br, and I) nanocrystals combined with the 2,5-diphenyloxazole (PPO) organic liquid [20], have been explored as scintillators for traditional X-ray [21], proton, or γ-ray imaging applications [22]. These perovskite scintillators have excellent light yield upon high energy radiation excitation, like X-ray or γ-ray. However, the synthesis of these halide perovskite nanocrystals produce a lot of toxic solvent solution which is expensive and time-consuming to deal with. Halide perovskite scintillators are generally hygroscopic.

* Corresponding authors.
E-mail addresses: lv_tianshuai@126.com, lv_tianshuai@hqu.edu.cn (T. Lyu), weizhanhua@hqu.edu.cn (Z. Wei).

https://doi.org/10.1016/j.cej.2023.141685
Received 4 November 2022; Received in revised form 24 January 2023; Accepted 31 January 2023
Available online 2 February 2023

Nitrogen filled glove box need to be carefully utilized during their synthesis processes. Particularly, the synthesized halide perovskite scintillators will decompose after exposure to water, air, or highly intense photon or ionizing radiation [3,23]. Their optical properties, like light yield, then deteriorate rapidly, limiting their commercial applications. This triggered our interest to develop novel perovskite phosphors with good optical properties and stability.

An afterglow or storage phosphor is an inorganic compound which can capture free electrons and holes in defects based traps during exposure to ionizing radiation like X-ray [24–27]. The stored electrons and holes can later be liberated via thermal or optical stimulation to yield light emission [28,29]. Because of this feature, storage phosphor has been utilized in various applications, for example, in light dosimeter for ultraviolet to infrared light detection [30], digital dental radiographic imaging setup [31,32], and X-ray computed tomography [24]. To date, BaFBr(I):Eu^{2+} is still the state-of-the-art X-ray storage phosphor [33]. However, the BaFBr(I):Eu^{2+} is hygroscopic. This is an on-going research to exploit new alternatives [26,34,35].

In ref. [14], a $NaLuF_4$:Tb(15 mol%)@$NaYF_4$ afterglow nanocrystal was reported. A sheet of flexible polymer plate was made by admixing the $NaLuF_4$:Tb(15 mol%)@$NaYF_4$ nanocrystals with the polydimethylsiloxane (PDMS) gel, which was tentatively utilized for demonstration of X-ray imaging of a curved circuit board. To realize commercially medical or industrial applications, several problems are required to be solved. Like halide perovskites and BaFBr(I):Eu^{2+}, the $NaLuF_4$:Tb(15 mol%)@$NaYF_4$ afterglow phosphor is hygroscopic, then limiting its durability. Since only a small amount of $NaLuF_4$:Tb(15 mol %)@$NaYF_4$ afterglow phosphor (~2% by weight) was dispersed in the polydimethylsiloxane gel based plate, there is room to increase the X-ray detection sensitivity of the plate by improving the charge carrier storage capacity of the utilized afterglow phosphor. More fundamentally, the defect(s) type and the charge carrier trapping and de-trapping processes in $NaLuF_4$:Tb(15 mol%) still remain unclear. Possibly, host unintended defects act as the electron trapping centre and then it is challenging to rationally improve its charge carrier storage capacity. To the best of our knowledge, reports on designing afterglow or storage phosphors for flexible X-ray imaging application are rare.

An afterglow or storage phosphor is generally constituted of a compound host lattice, charge carrier capturing centres, and the recombination centres [36]. The trapping depths of the electron and hole capturing centres and their atomic distribution within the compound crystal determine the duration that the charge carriers are trapped in traps [26]. For afterglow phosphor, about 0.6 eV deep trapping depth is required. For storage phosphor, larger than ~ 0.8 eV deep trapping depth is needed in order to prevent thermal fading of stored charge carriers from traps at room temperature (RT). To rationally develop an afterglow or storage phosphor, knowledge on the energy level locations of electron and hole capturing centres in a compound is crucial to design trapping depths [37]. In ref. [38], a chemical shift model has been developed in 2012 to construct a vacuum referred binding energy (VRBE) diagram for lanthanide doped inorganic compounds. In a VRBE diagram, the binding energy of an electron in different impurity states can be compared with respect to a common reference energy [25,39–41].

Like $LiNbO_3$ and $NaTaO_3$, lithium tantalate ($LiTaO_3$) is a perovskite compound with a *R*3*c* crystal space group. $LiTaO_3$ crystal combines good chemical stability, special electro-optical, and piezoelectric properties, which allow it to have many applications, like in photocatalysts [42], lithium-ion batteries [43], and optical waveguide [44]. Particularly, $LiTaO_3$ has a very high density (about 7.5 g/cm^3) which is even higher than that of BaFBr (about 5 g/cm^3) [24]. It then has a high absorption coefficient of X-rays which is a necessity for a promising compound.

In ref. [45], a photochromic phenomenon was observed in $LiTaO_3$:Bi^{3+},Dy^{3+} persistent luminescence phosphor. In ref. [46], a mechanoluminescence phenomenon was observed in $LiTaO_3$:Bi^{3+},Tb^{3+},Ga^{3+},Ge^{4+} afterglow phosphor. However, both the $LiTaO_3$:Bi^{3+},Dy^{3+} and $LiTaO_3$:Bi^{3+},Tb^{3+},Ga^{3+},Ge^{4+} compounds were developed by a trial-and-error method and the charge carrier trapping processes are not fully clear. To address this issue, spectroscopic and thermoluminescence properties of lanthanides and bismuth doped $LiTaO_3$ perovskite were carefully studied to establish the so-called vacuum referred binding energy (VRBE) diagram of $LiTaO_3$ in ref. [47] which has been reproduced in Fig. 1(a). However, it has not been fully utilized to explore X-ray charged storage phosphor for flexible X-ray imaging of curved objects. Particularly, it still remains unknown whether Eu^{3+} can really work as a good electron capturing centre or not in $LiTaO_3$. In ref. [47], the charge carrier trapping properties of Bi^{3+} was studied and it was found that its electron trapping depth was too shallow for stable electron storage. The VRBE diagram in Fig. 1(a) predicts that Eu^{3+} provides a 0.5 eV deeper trap. This was the motivation to combine the potential ~ 1.1 eV deep electron trapping Eu^{3+} with the ~ 1.5 eV deep hole trapping defect Pr^{3+} or Tb^{3+} in $LiTaO_3$ in this work.

We will demonstrate that Eu^{3+} indeed acts as a deeper electron trapping centre than Bi^{3+} for designing good storage phosphor. The ratios denoted as (r1; r2; r3) of the integrated thermoluminescence (TL) intensity of the optimized $LiTaO_3$:0.005Tb^{3+},0.001Eu^{3+} to that of the state-of-the-art (r1) BaFBr(I):Eu^{2+}, (r2) Al_2O_3:C, or (r3) $NaLuF_4$:Tb^{3+} are 5.2, 8.8, or 2.8, respectively. The charge carriers can be stored more than 1000 h in $LiTaO_3$:0.005Tb^{3+},0.001Eu^{3+}. The storage capacity after X-ray charging in the rationally designed $LiTaO_3$:0.005Tb^{3+},0.001Eu^{3+} are much higher than that in previously reported $LiTaO_3$:Bi^{3+},Dy^{3+}, $LiTaO_3$:Bi^{3+}, and $LiTaO_3$:Bi^{3+},Tb^{3+} storage phosphors developed by a trial-and-error approach. $LiTaO_3$ is an oxide based compound which is synthesized at high temperature (1200 °C). It then has better chemical stability compared with halide compounds which are hygroscopic, for instance, the BaFBr. We will demonstrate that the synthesized $LiTaO_3$:0.005Tb^{3+},0.001Eu^{3+} storage phosphor indeed has good chemical stability during exposure to water.

We will further demonstrate that the charge carriers stored in $LiTaO_3$:0.005Tb^{3+},0.001Eu^{3+} can be efficiently liberated by a wide range energy photon stimulation from 365 nm UV-light (3.4 eV) to 905 nm infrared laser (1.4 eV). Proof-of-concept anti-counterfeiting application will be demonstrated by combining the colour-tailorable photoluminescence, afterglow, thermally, or optically stimulated luminescence in $LiTaO_3$:0.005Tb^{3+},xEu^{3+} and $LiTaO_3$:0.005Pr^{3+},0.001Eu^{3+}. Advanced multimode anti-counterfeiting applications will be proposed by combining a high absolute X-ray scintillation light yield of 19000 ± 1800 ph/MeV of $LiTaO_3$:0.005Tb^{3+},0.001Eu^{3+}. Proof-of-concept flexible X-ray imaging application will be demonstrated by using the optimized $LiTaO_3$:0.005Tb^{3+},0.001Eu^{3+} based silicone gel film as shown in Fig. 1 (b), which is not reported in our previous studies.

2. Experimental

The utilized Li_2CO_3 (99.99 %) was purchased from Shanghai Macklin Biochemical company. Other starting chemicals including the BaF_2 crystal powder with a high purity of 99.99 % were bought from Shanghai Aladdin chemical company. Compounds were synthesized by employing a typical high-temperature solid-state reaction technique. The appropriate stoichiometric mixture of Bi_2O_3 (99.99 %), Pr_6O_{11} (99.99 %), Tb_4O_7 (99.99 %), Eu_2O_3 (99.99 %), Li_2CO_3 (99.99 %), and Ta_2O_5 (99.99 %) was carefully weighted based on the designed compound compositions. The mixture was then homogeneously mixed in an agate mortar with a pestle and acetone solution for ~20 min in a fume hood. The well mixed powder mixture was then placed in a covered corundum crucible, which was kept first at 800 °C for 2 h and then at 1200 °C for 6 h under ambient atmosphere. A heating rate of 5 °C per minute was utilized for the tube furnace. After that, the prepared $LiTaO_3$ compounds were cooled to room temperature (RT), which were then ground and mixed well prior to further measurements. To optimize the thermoluminescence intensity of $LiTaO_3$:0.005Tb^{3+}, 0.001Eu^{3+}, it was synthesized at 1250 °C with a duration of 6 h and the utilized heating

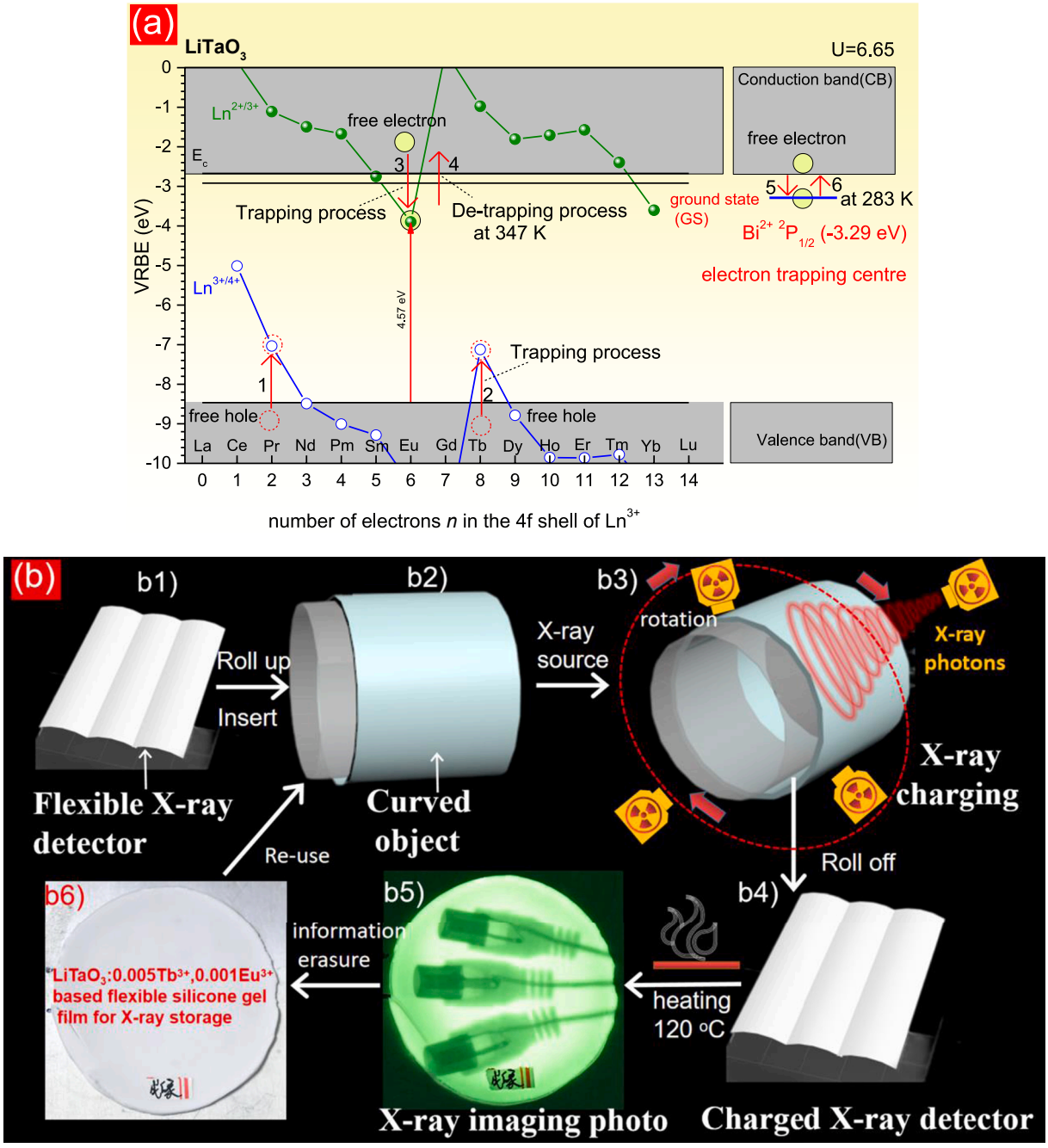

Fig. 1. (a) Vacuum referred binding energy (VRBE) diagram of $LiTaO_3$. The VRBEs in the ground states of Bi^{2+}, divalent, and trivalent lanthanides are shown. Charge carrier trapping and release processes denoted by red arrows will be explained in the text. (b1) until (b6) Illustration on how to realize flexible X-ray imaging application by utilizing the $LiTaO_3$:0.005Tb^{3+},0.001Eu^{3+} dispersed in a silicone gel film. (For interpretation of the references to colour in this figure legend, the reader is referred to the web version of this article.)

rate for the tube furnace is 3 °C per minute. To demonstrate flexible X-ray imaging application as shown in Fig. 1(b), the optimized $LiTaO_3$:0.005Tb^{3+},0.001Eu^{3+} powder phosphor was first sieved by a 300 mesh screen. About 0.65 g sieved phosphor was dispersed in 4.40 g silicone gel (Sylgard 184, Dow Corning) to synthesize a highly elastic film with a diameter of ~ 7 cm. The film was kept at about 75 °C for about 4 h in vacuum. For the afterglow and X-ray imaging photographs, an iPhone 12Pro or a digital Nikon D850 camera was utilized.

All prepared compounds were first identified by utilizing a Japan Rigaku Smar/SmartLa X-ray diffraction facility. It is equipped with an X-ray tube worked at 40 kV and 30 mA. The scanning electron microscope (SEM) photographs and energy dispersive X-ray spectroscopy (EDX) measurements for the as-synthesized $LiTaO_3$ were recorded with a Japan JEOL JSM-7610FPlus electron microscope. Transmission electron microscope (TEM) photographs were recorded by a FEI/ Talos F200X G2 (Enfinium SE 976). X-ray excited emission spectra of $LiTaO_3$:0.005Tb^{3+},0.001Eu^{3+} and BaF_2 crystal powder were measured by an Edinburgh FS5 spectrofluorometer (Edinburgh Instruments Ltd.). It contains an X-ray tube (AMPTEK Ltd.), which were operated at 50 KV and 70 μA. $LiTaO_3$:0.005Tb^{3+},0.001Eu^{3+} or BaF_2 was pressed into a pill with 0.6 cm diameter and 3 mm thickness and the entire surface was irradiated by the X-rays. The measured X-ray excited emission spectra were corrected by the detection sensitivity of emission light and X-ray excitation time. A FLS920 fluorescence spectrometer (Edinburgh

Instruments Ltd.) has been utilized to measure the room temperature (RT) photoluminescence excitation (PLE) spectra, emission spectra (PL), RT (~298 K) isothermal decay curves, and afterglow spectra after Hg lamp (254 nm UV-light) charging in the dark. We have corrected the recorded PLE spectra by using the wavelength-dependent excitation intensity of the used xenon lamp in the FLS920 facility.

X-ray excited integrated emission intensity from about 250 to 700 nm as a function of time, above 100 K or 300 K thermoluminescence (TL) emission (TLEM) spectra, TL glow curves, and RT isothermal decay curves after X-ray or 254 nm UV-light charging were recorded with a facility. It contains a QE65Pro spectrometer (Ocean Optics Ltd.), a TUB00083-2 X-ray tube (MOXTEK, Ltd.), a thermostat operated in the temperature range between 100 and 600 K, a thermostat operated in the temperature range between 300 and 773 K, a SCHOTT BG-39 filter, a Hg lamp (254 nm UV-light), and a Hamamatsu R928P photomultiplier tube. For optically stimulated luminescence study, we employed different energy stimulation light source, like 850 nm (1.5 eV) infrared laser, 656 nm (1.9 eV) red laser, a commercial white light-emitting-diode (WLED, 52 mW/cm^2), a 396 nm (3.1 eV) light-emitting diode (LED), and a 365 nm (3.4 eV) ultraviolet lamp. Prior to all measurements, all compounds were placed in a nitrogen atmosphere and then kept at 450 °C with a duration of 120 s to remove stored charge carriers from all traps in the dark. After that, the samples were cooled to 100 K for above 100 K TL measurements or cooled to room temperature (RT, ~298 K) for above RT TL measurements. Traditional TL glow curves were corrected by both the sample mass and the X-ray or 254 nm UV-light charging time.

To unravel charge carrier trapping and liberation processes, we measured thermoluminescence excitation (TLE) curves [34,48,49] for $LiTaO_3$:0.005Tb^{3+},0.001Eu^{3+} and $LiTaO_3$:0.005Pr^{3+},0.001Eu^{3+} by utilizing the FLS920 fluorescence spectrometer (Edinburgh Instruments Ltd.) equipped with a single-grating excitation monochromator and a 450 W xenon arc lamp. Afterglow phosphor was first charged by different energy photons in the spectral range between 200 nm (6.2 eV) and 400 nm (3.1 eV) for 60 s and then RT isothermal decay curves were recorded during 60 s. The monitored wavelength is λ_{em} = 544 nm for $LiTaO_3$:0.005Tb^{3+},0.001Eu^{3+} and λ_{em} = 614 nm for $LiTaO_3$:0.005Pr^{3+},0.001Eu^{3+}. A so-called TL excitation curve was constructed by plotting the corrected room temperature integrated decay intensity as a function of excitation wavelength in the range between 200 and 400 nm.

3. Results

3.1. Photoluminescence, X-ray excited emission, and afterglow properties in $LiTaO_3$:Ln^{3+},Eu^{3+} (Ln = Tb or Pr)

Fig. 2(a) and Fig. S4 show the PLE (λ_{em} = 614 or 623 nm) and PL (λ_{ex} = 272 or 300 nm) spectra of $LiTaO_3$:0.005Pr^{3+},0.001Eu^{3+}. Like in our previous study in ref. [47], the excitation band peaked at about 267 nm is attributed to electron transfer from the $LiTaO_3$ valence band (VB) top to Eu^{3+}, i.e., VB → Eu^{3+} charge transfer (CT) [50]. The broad excitation band peaked at ~288 nm is attributed to the Intervalence Charge Transfer Band (IVCT) because of electron transfer from the Pr^{3+} 4f ground state to the $LiTaO_3$ conduction band (CB) bottom, i.e., Pr^{3+}→CB IVCT [47]. The line excitation bands in the spectral range from 350 to 550 nm are due to characteristic 4f → 4f transitions of Eu^{3+} and Pr^{3+}. Upon 272 or 300 nm excitation, characteristic 4f → 4f emissions of Pr^{3+} and Eu^{3+} appear (Fig. S4). More than 50 min of Pr^{3+} 4f → 4f afterglow is measurable after 254 nm UV-light charging (Fig. S6).

Fig. 2(b) shows the PLE (λ_{em} = 544 or 623 nm) and PL (λ_{ex} = 269 or 285 nm) spectra of $LiTaO_3$:0.005Tb^{3+},0.001Eu^{3+}. Based on the study in ref. [47], the excitation band peaked at ~ 231 nm in Fig. 2(a) and at ~ 226 nm in Fig. 2(b) is attributed to the $LiTaO_3$ host exciton creation (E^{ex}) at RT. A common excitation band peaked at ~ 249 nm appears in Fig. 2 (b), which was also observed in $LiTaO_3$ host, Bi^{3+} and/or lanthanides doped $LiTaO_3$ compounds in ref. [47]. It is therefore attributed to host-related intrinsic defect(s). The excitation band peaked at ~ 268 nm is attributed to the VB → Eu^{3+} charge transfer band and the broad excitation band peaked at ~ 285 nm is attributed to Tb^{3+}→CB IVCT. The line excitation bands in the spectral range from 350 to 400 nm are due to the Eu^{3+} 4f → 4f transitions. Upon 254 nm excitation, $LiTaO_3$:0.005Tb^{3+},0.001Eu^{3+} shows intense Tb^{3+} $^5D_4$→^7F_j (j=0–6) emissions (Fig. 2(b)). The optical properties of $LiTaO_3$:0.005Tb^{3+},xEu^{3+} were further studied in Figs. S8-S11.

Fig. 2(c) shows the X-ray excited emission spectra of $LiTaO_3$:0.005Tb^{3+},0.001Eu^{3+} and BaF_2 measured at RT. BaF_2 is a well-known scintillating material that shows a broad self-trapped-exciton emission band peaked at ~ 314 nm upon X-ray excitation and has an absolute scintillation light yield of about 10000 ph/MeV (photons yielded per 10^6 eV of absorbed X-ray energy)[51–53]. BaF_2 was therefore utilized as a reference to estimate the absolute X-ray excited emission intensity for $LiTaO_3$:0.005Tb^{3+},0.001Eu^{3+}. The emission spectrum of $LiTaO_3$:0.005Tb^{3+},0.001Eu^{3+} upon X-ray excitation is composed of Tb^{3+} $^5D_4$→^7F_j transitions in Fig. 2(c), which is consistent with that upon ultraviolet light excitation in Fig. 2(b). The absolute scintillation light yield of $LiTaO_3$:0.005Tb^{3+},0.001Eu^{3+} was calculated to be about 19000 ± 1800 ph/MeV by using the ratio of its integrated emission intensity from 200 to 800 nm to that of the BaF_2 (10000 ph/MeV) reference.

The absolute scintillation light yield of $LiTaO_3$:0.005Tb^{3+},0.001Eu^{3+} is about 0.5 and 2.3 times higher than that of the commercial scintillators NaI:Tl (38000 ph/MeV) and $Bi_4Ge_3O_{12}$ (8200 ph/MeV) [52,54].

Fig. 2(d) shows the 2D contour plot of room temperature isothermal afterglow spectra for $LiTaO_3$:0.005Tb^{3+},0.001Eu^{3+} after 254 nm UV-light charging. The afterglow spectrum is composed of characteristic Tb^{3+} $^5D_4$→^7F_j emissions, indicating that Tb^{3+} is the recombination and luminescence centre. More than 35 min of Tb^{3+} $^5D_4$→^7F_j afterglow is measurable.

To understand electron and hole capturing and release processes, thermoluminescence excitation (TLE) plots of Eu^{3+} and Ln^{3+} (Ln = Tb or Pr) doped $LiTaO_3$ were recorded. Fig. 2(e) and (f) show the room temperature isothermal decay curves of $LiTaO_3$:0.005Tb^{3+},0.001Eu^{3+} and $LiTaO_3$:0.005Pr^{3+},0.001Eu^{3+} after different energy photon charging in the dark. Fig. 2(g) and (h) compare the thermoluminescence excitation (TLE) plots with the photoluminescence excitation spectra of $LiTaO_3$:0.01 Tb^{3+}, $LiTaO_3$:0.005Eu^{3+}, or $LiTaO_3$:0.01Pr^{3+}. The $LiTaO_3$:0.005Tb^{3+}, 0.001Eu^{3+} and $LiTaO_3$:0.005Pr^{3+},0.001Eu^{3+} afterglow phosphors emerge to be filled by optical excitation of the intrinsic defect(s), Tb^{3+}→CB IVCT, or Pr^{3+}→ CB IVCT. Note that the Eu^{3+} charge transfer band does not appear in the charging spectra indicating that VB hole generation is not involved in the charging process.

3.2. Eu^{3+} acts as an electron trap for designing $LiTaO_3$:Ln^{3+},Eu^{3+} (Ln = Tb or Pr) storage phosphor

To unravel the nature of the recombination and luminescence centre during TL read-out, thermoluminescence emission (TLEM) spectra were recorded for Ln^{3+},Eu^{3+}-codoped $LiTaO_3$ (Ln = Pr or Tb). Fig. 3(a) shows the 2D contour plot of above 100 K TLEM spectra of $LiTaO_3$:0.005Pr^{3+},0.001Eu^{3+} measured at β = 2 K/s after X-ray charging. Characteristic Pr^{3+} 4f → 4f emissions from visible to near infrared (450 nm until 950 nm) with a main TL glow band peaked at ~ 361 K emerge. Since no obvious TL glow peaks appear below 300 K in Fig. 3(a), TLEM spectra for $LiTaO_3$:0.005Tb^{3+},0.001Eu^{3+} were measured above 300 K. Fig. 3(b) shows the 2D contour plot of above 300 K TLEM spectra of $LiTaO_3$:0.005Tb^{3+},0.001Eu^{3+} recorded at a heating rate of 1.2 K/s after X-ray charging. Characteristic Tb^{3+} $^5D_4$ → ^7F_j emissions with a broad TL glow band peaked at about 352 K and extending from 300 to 500 K appear.

Fig. 3(c) compares the above 305 K TL glow curves of Ln^{3+} or/and Eu^{3+} (Ln = Tb or Pr) doped $LiTaO_3$ measured at a heating rate of 1 K/s after X-ray charging. Compared with $LiTaO_3$:0.005Pr^{3+} in Fig. 3(c1) or

$LiTaO_3$:0.005Tb^{3+} in Fig. 3(c3), a new common thermoluminescence glow band peaked at ~ 347 K appears in $LiTaO_3$:0.005Pr^{3+},0.001Eu^{3+} in Fig. 3(c2) and $LiTaO_3$:0.005Tb^{3+},0.001Eu^{3+} in Fig. 3(c4) where Pr^{3+} or Tb^{3+} acts as the recombination and luminescence centre. It will be assigned to electron liberation from Eu^{2+} to recombine with holes captured at Pr^{4+} or Tb^{4+}, yielding typical emissions of Pr^{3+} or Tb^{3+} during TL read-out. In Fig. 3(c1), two TL glow bands peaked at about 397 and 468 K appear in $LiTaO_3$:0.005Pr^{3+}. They also emerge in

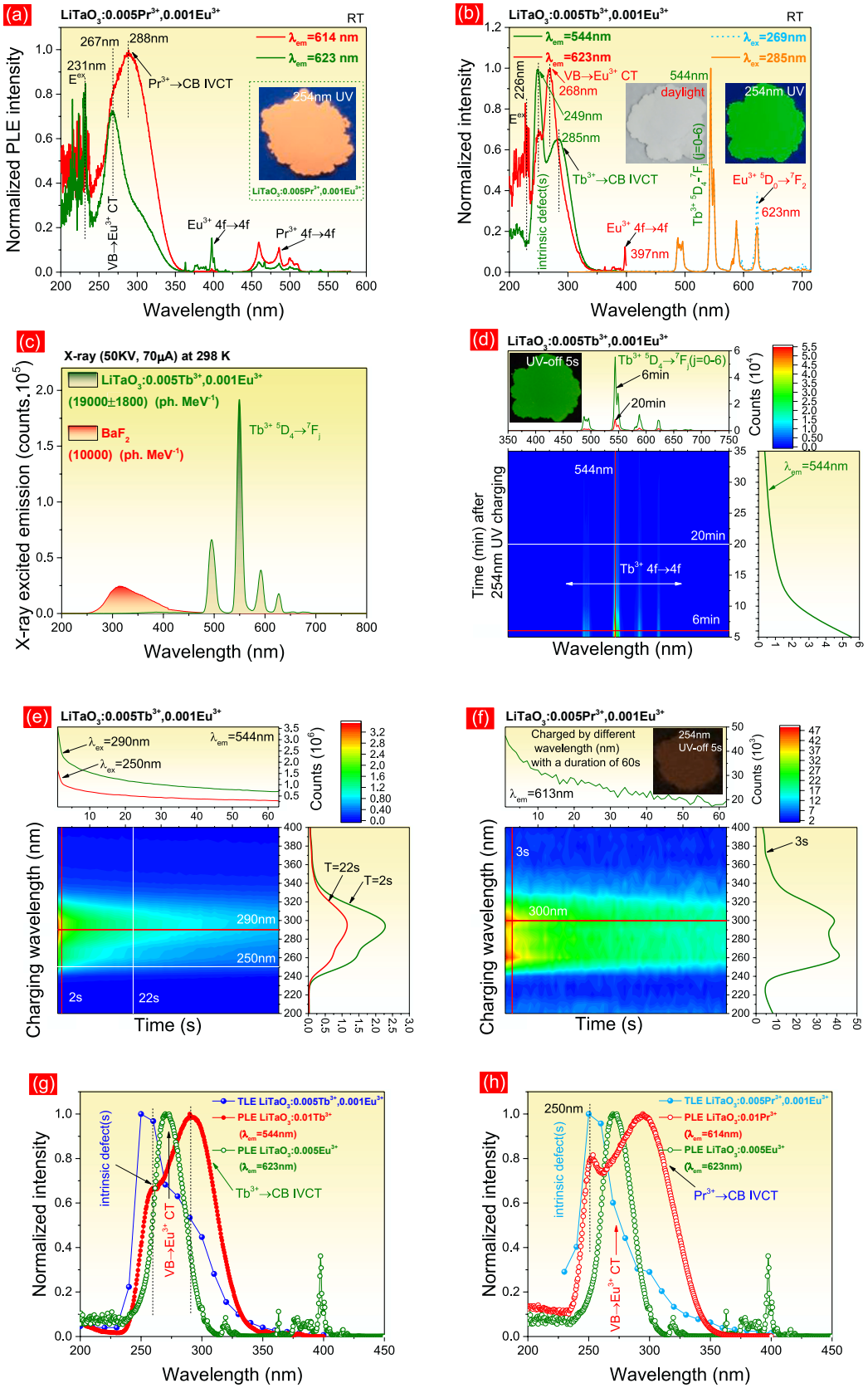

Fig. 2. PLE and PL spectra of (a) $LiTaO_3$:0.005Pr^{3+},0.001Eu^{3+} and (b) $LiTaO_3$:0.005Tb^{3+},0.001Eu^{3+}. (c) X-ray excited emission spectra of $LiTaO_3$:0.005Tb^{3+},0.001Eu^{3+} and the commercial BaF_2. (d) RT isothermal afterglow spectra of $LiTaO_3$:0.005Tb^{3+}, 0.001Eu^{3+} after 254 nm UV-light charging. RT isothermal decay curves of (e) $LiTaO_3$:0.005Tb^{3+},0.001Eu^{3+} and (f) $LiTaO_3$:0.005Pr^{3+}, 0.001Eu^{3+} after different energy photon excitation for 60 s. (g) and (h) A comparison of thermoluminescence excitation (TLE) curves with the photoluminescence excitation spectra of Tb^{3+}, Eu^{3+}, or Pr^{3+} doped $LiTaO_3$.

$LiTaO_3$:0.005Pr^{3+},0.001Eu^{3+} in Fig. 3(c2). In Fig. 3(c3), two broad TL glow bands peaked at about 397 and 447 K emerge in $LiTaO_3$:0.005Tb^{3+}. The two TL peaks also appear in $LiTaO_3$:0.005Tb^{3+},0.001Eu^{3+} in Fig. 3(c4). The 397, 447, and 468 K will be then assigned to host-related intrinsic electron trapping centres.

3.3. Eu^{3+} acts as an excellent electron trap for obtaining high charge carrier storage capacity in $LiTaO_3$:0.005Tb^{3+},xEu^{3+}

The effect of Eu^{3+} concentration on the charge carrier storage capacity was studied in $LiTaO_3$:0.005Tb^{3+},xEu^{3+}. Fig. 4(a1) shows the TL

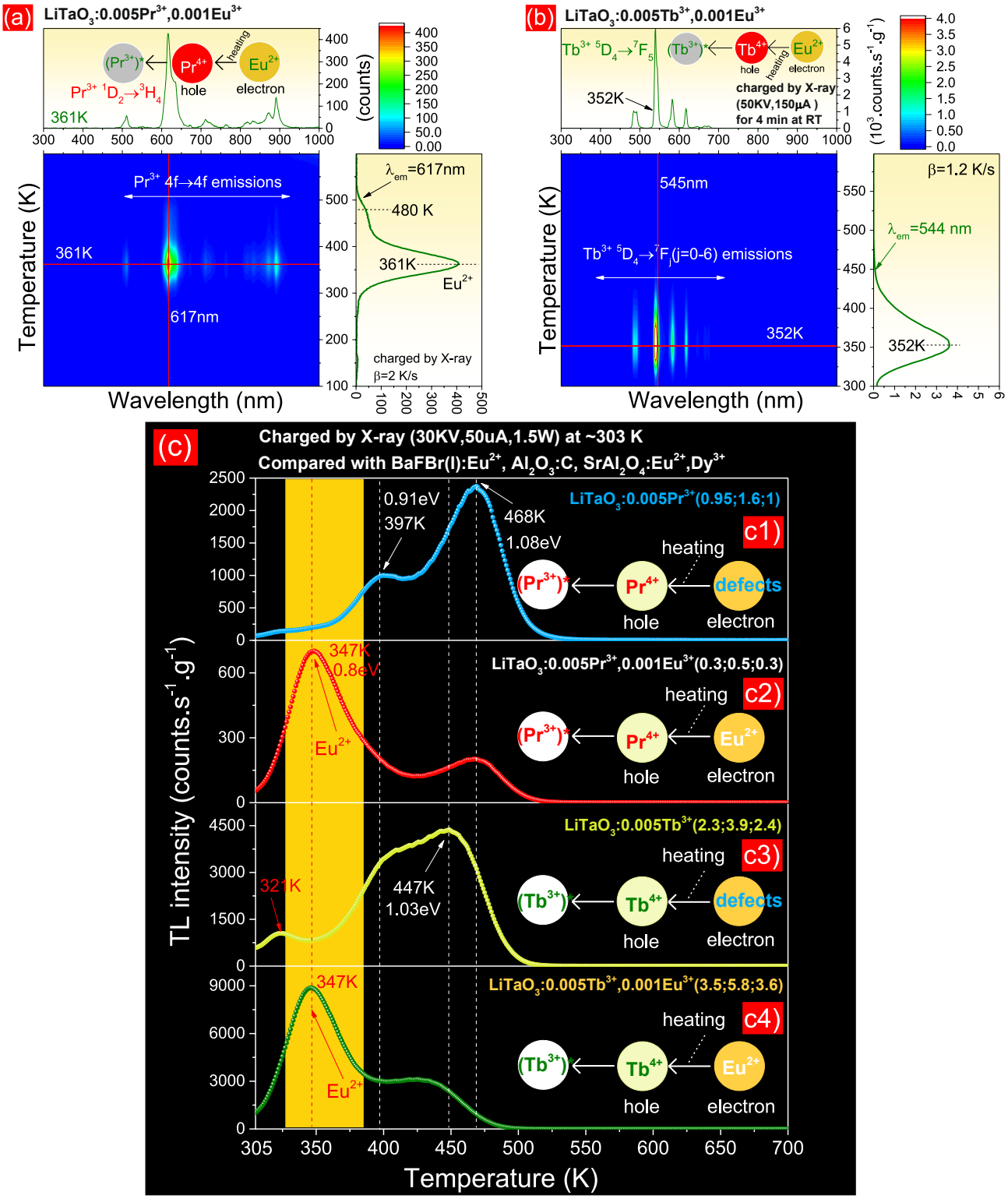

Fig. 3. (a) Above 100 K TLEM spectra of $LiTaO_3$:0.005Pr^{3+},0.001Eu^{3+} and (b) above 300 K TLEM spectra of $LiTaO_3$:0.005Tb^{3+},0.001Eu^{3+} after X-ray charging. (c1) until (c4) TL glow curves of Ln^{3+} or/and Eu^{3+} (Ln = Tb or Pr) doped $LiTaO_3$ charged by X-rays. The ratios of TL intensities of Tb^{3+}, Pr^{3+}, or Eu^{3+} co-doped $LiTaO_3$ to that of the commercial BaFBr(I):Eu^{2+}, Al_2O_3:C chip, or $SrAl_2O_4$:Eu^{2+},Dy^{3+} are shown in the legend in panel (c). The Pr^{3+} emissions in (c1) and (c2) and the Tb^{3+} emissions in (c3) and (c4) were monitored during TL-readout.

glow curves of $LiTaO_3$:0.005Tb^{3+},xEu^{3+} (x = 0.0005 until 0.006) after 254 nm UV-light charging. A TL glow band peaked at about 350 K appears. Its integrated TL intensity from 303 to 700 K gradually decreases from x = 0.0005 until x = 0.006. Fig. 4(b) shows the TL glow curves of $LiTaO_3$:0.005Tb^{3+},xEu^{3+} after X-ray charging. The ratios (r1; r2; r3) of integrated TL intensity of $LiTaO_3$:0.005Tb^{3+},xEu^{3+} to that of the commercial (r1) BaFBr(I):Eu^{2+}, (r2) Al_2O_3:C chip, or (r3) $SrAl_2O_4$:Eu^{2+},Dy^{3+}, are shown in the legends of Fig. 4(a1) and 4(b), respectively. A TL glow band peaked at about 346 K emerges. Its integrated TL intensity increases from x = 0.0005 to x = 0.001, and then rapidly decreases with further increasing x.

Fig. 4(c) compares the TL glow curves of Bi^{3+}, Tb^{3+} doped, and Tb^{3+} plus Eu^{3+} doped $LiTaO_3$ after X-ray charging. We obtained and used the optimized afterglow $NaLuF_4$:Tb^{3+}(15 mol%) @$NaYF_4$ nanocrystals, abbreviated as $NaLuF_4$:Tb^{3+}, as synthesized by the authors in ref. [14] for comparison study. The ratios (r1; r2; r3) of the integrated TL intensity from 305 to 700 K of the Bi^{3+} and/or Ln^{3+} (Ln = Tb or Eu) doped $LiTaO_3$ and the $NaLuF_4$:Tb^{3+} to that of the commercial (r1) BaFBr(I):Eu^{2+}, (r2) Al_2O_3:C chip, (r3) $SrAl_2O_4$:Eu^{2+},Dy^{3+}, respectively, are shown in the legend of Fig. 4(c). Compared with $LiTaO_3$:0.005Bi^{3+}, $SrAl_2O_4$:Eu^{2+},Dy^{3+}, or $NaLuF_4$:Tb^{3+} afterglow phosphor, $LiTaO_3$:0.005Tb^{3+},0.001Eu^{3+} shows less intense TL intensity at 305 K. It

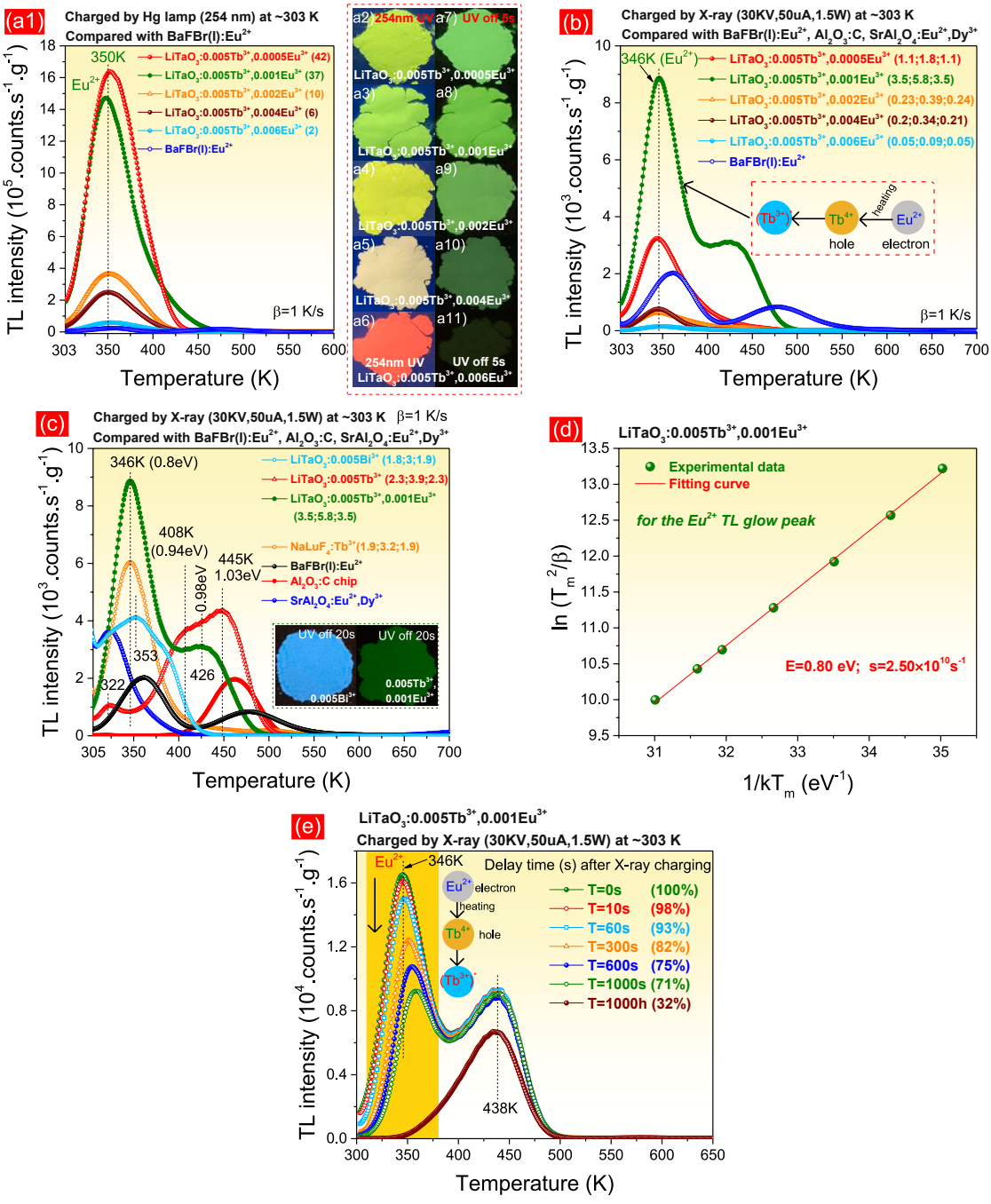

Fig. 4. TL glow curves of $LiTaO_3$:0.005Tb^{3+},xEu^{3+} charged by (a1) 254 nm UV-light or (b) X-rays. Photographs for $LiTaO_3$:0.005Tb^{3+},xEu^{3+} ((a2) until (a6)) upon or ((a7) until (a11)) after 254 nm UV-light illumination. (c) TL glow curves for Bi^{3+} and/or Ln^{3+} (Ln = Eu, Tb, or Pr) doped $LiTaO_3$ charged by X-rays. (d) A variable heating rate plot for $LiTaO_3$:0.005Tb^{3+},0.001Eu^{3+}. (e) Fading of TL glow curves of $LiTaO_3$:0.005Tb^{3+},0.001Eu^{3+} after X-ray charging and with different delay time from 0 until 1000 h. The ratios (r1; r2; r3) of integrated TL intensities from 303 to 700 K of Bi^{3+} and/or Ln^{3+} doped $LiTaO_3$ to that of the commercial (r1) BaFBr(I):Eu^{2+}, (r2) Al_2O_3:C chip, or (r3) $SrAl_2O_4$:Eu^{2+},Dy^{3+} are shown in the legends in panels (a1), (b), and (c), respectively.

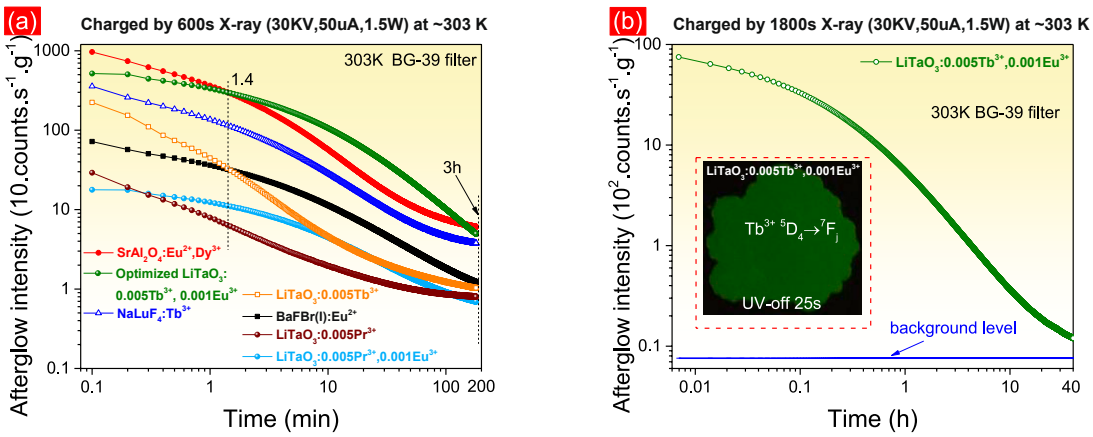

Fig. 5. (a) 3 h and (b) 40 h RT isothermal decay curves of Eu^{3+} and/or Ln^{3+} (Ln = Tb or Pr) doped $LiTaO_3$ after X-ray charging. The afterglow intensities in panels (a) and (b) were corrected by sample mass and X-ray charging time. The inset in panel (b) shows an afterglow photograph of $LiTaO_3$:0.005Tb^{3+},0.001Eu^{3+} recorded at 25 s after 254 nm UV-light charging.

means that $LiTaO_3$:0.005Tb^{3+},0.001Eu^{3+} has less intense initial afterglow at about RT, as demonstrated by the afterglow photographs in the insets of Fig. 4(c). Since the rationally designed $LiTaO_3$:0.005Tb^{3+},0.001Eu^{3+} has excellent charge carrier storage capacity, it has been studied further in detail.

We estimate the trapping depths for $LiTaO_3$:0.005Tb^{3+},0.001Eu^{3+} by utilizing a typical variable heating rate plot as shown in Fig. 4(d) and the following equation [26,55–58]:

$$\ln\left(\frac{T_m^2}{\beta}\right) = \frac{E}{kT_m} + \ln\left(\frac{E}{ks}\right) \quad (1)$$

where β denotes the used heating rate, E means the trapping depth, T_m is the temperature of a TL glow peak maximum, s means the frequency factor, and k is the well-known Boltzmann constant (8.62×10^{-5} eV/k). The fitting of results in Fig. 4(d) provides a frequency factor of $s = 2.50 \times 10^{10}$ s^{-1} and an electron capturing depth of 0.80 eV for the 346 K TL glow peak of $LiTaO_3$:0.005Tb^{3+},0.001Eu^{3+} in Fig. 4(c). The electron trap depths of other thermoluminescence glow peaks were estimated and provided in the legend of Fig. 3(c) and Fig. 4(c) by utilizing Eq. (1) with $s = 2.50 \times 10^{10}$ s^{-1}, β = 1 K/s, and the observed T_m values.

Fig. 4(e) shows the TL glow curves of $LiTaO_3$:0.005Tb^{3+},0.001Eu^{3+} after X-ray charging and then followed by fading in the dark with different duration from 0 until 1000 h. The TL glow band peaked at ~ 346 K gradually decreases with increasing fading time. The ratios of the integrated TL intensity with different duration fading to that of without fading are shown as the percentage values in the legend of Fig. 4(e). After 60 s, 1000 s, or 1000 h fading, the integrated TL intensity of $LiTaO_3$:0.005Tb^{3+},0.001Eu^{3+} remains 93 %, 71 %, or 32 %. The similar applied to $LiTaO_3$:0.005Pr^{3+},0.001Eu^{3+} in Fig. S20.

Fig. 5(a) shows the RT isothermal decay curves of Ln^{3+} doped $LiTaO_3$ after 600 s X-ray charging. Compared with $SrAl_2O_4$:Eu^{2+},Dy^{3+}, the optimized $LiTaO_3$:0.005Tb^{3+},0.001Eu^{3+} shows less intense initial afterglow intensity. Fig. 5(b) shows that more than 40 h Tb^{3+} $^5D_4 \rightarrow {}^7F_j$ afterglow can be measurable in $LiTaO_3$:0.005Tb^{3+},0.001Eu^{3+} after 1800 s X-ray charging.

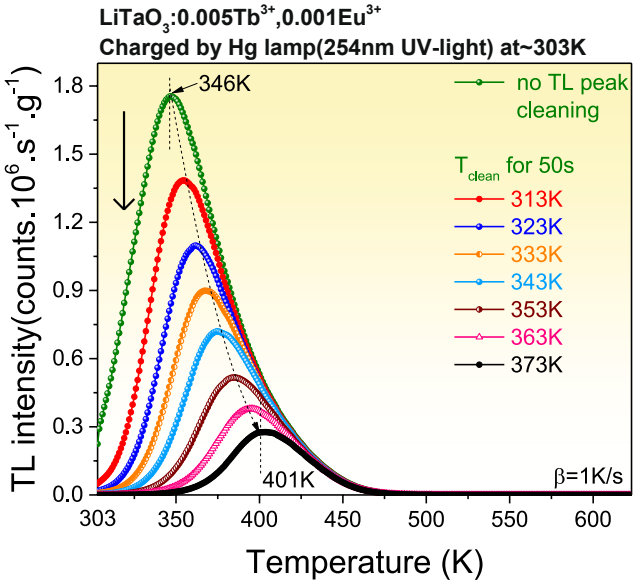

Fig. 6. TL glow curves for $LiTaO_3$:0.005Tb^{3+},0.001Eu^{3+} measured at β = 1 K/s after 254 nm UV-light charging and then followed by a TL glow peak cleaning at T_{clean} for 50 s.

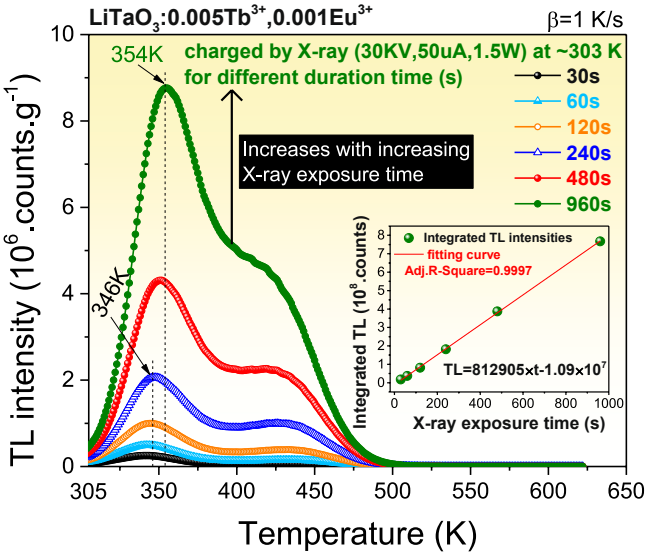

Fig. 7. TL glow curves of $LiTaO_3$:0.005Tb^{3+},0.001Eu^{3+} charged by X-rays with different duration. The inset shows the integrated TL intensities between 305 and 623 K as a function of X-ray exposure time.

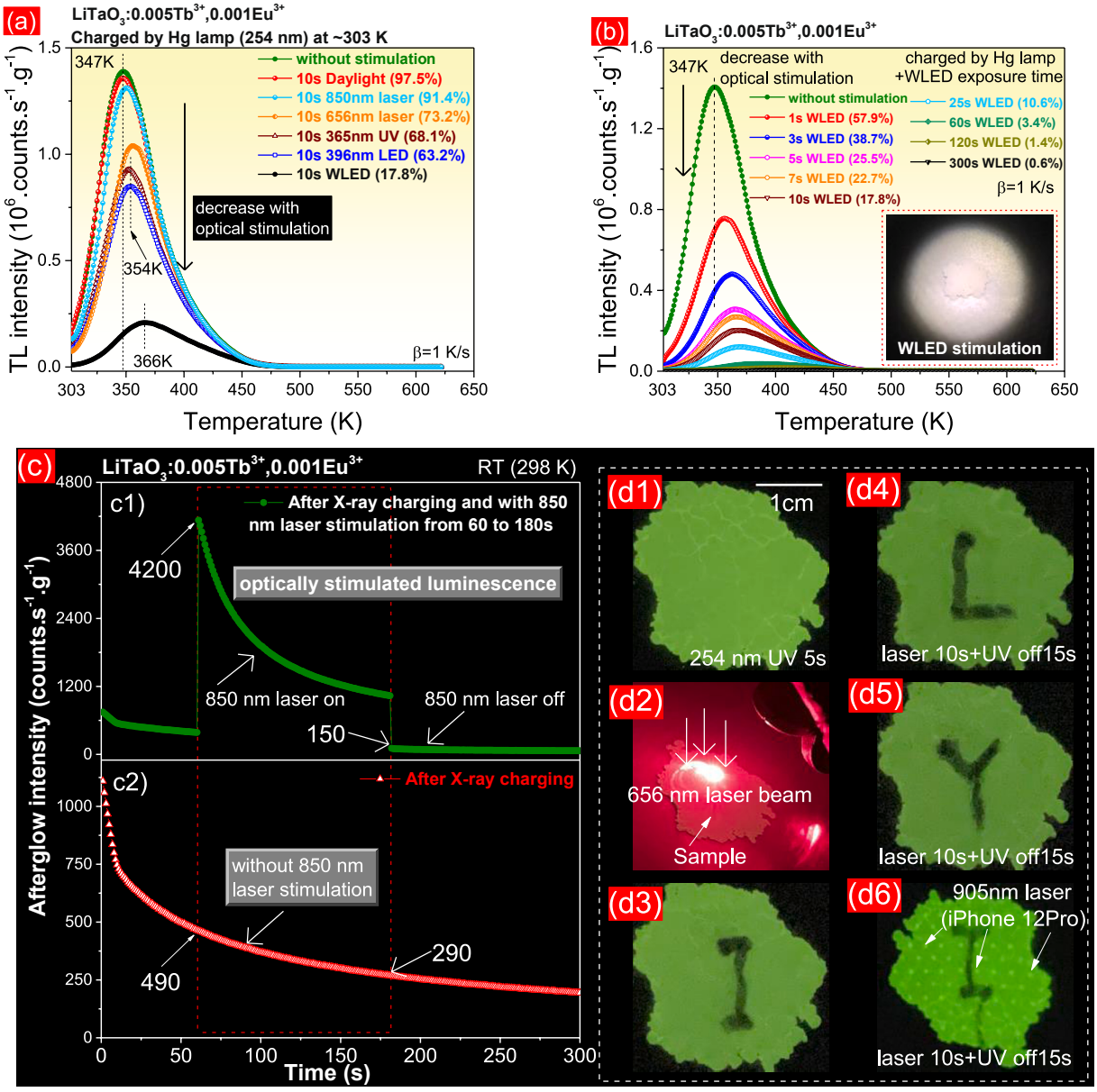

Fig. 8. TL glow curves of $LiTaO_3$:0.005Tb^{3+},0.001Eu^{3+} charged by 254 nm UV-light and then followed by (a) different energy photon stimulation and (b) WLED stimulation with different duration time. (c) RT isothermal decay curves after X-ray charging and then followed by 850 nm stimulation for 120 s. (d1) until (d6) Information display of "I", "L", and "Y" by utilizing the Tb^{3+} afterglow and liberating stored charge carriers with 656 or 905 nm laser optically stimulated emission properties in $LiTaO_3$:0.005Tb^{3+},0.001Eu^{3+}.

4. Discussion: Unraveling Eu^{3+} as a deep electron trap

The VRBE diagram of $LiTaO_3$ in Fig. 1(a) predicts that Bi^{3+} or Eu^{3+} act as ~ 0.6 or ~ 1.1 eV deep electron traps, while Tb^{3+} or Pr^{3+} acts as ~ 1.4 or ~ 1.5 eV deep hole traps. In ref. [47], the dual role of Bi^{3+} in capturing electrons and holes was studied in bismuth doped $LiTaO_3$. As demonstrated in Fig. 4 in ref. [47], electron liberation from Bi^{2+} and recombination with the hole trapped at Bi^{4+} leads to the Bi^{3+} emission with a TL glow peak at about 283 K. Its estimated electron trap depth is ~ 0.65 eV. Apparently, the Bi^{3+} electron trap depth (~0.65 eV) is not deep enough to design a stable storage phosphor which is operated at room temperature. The predicted electron capturing depth of Eu^{3+} is about 0.5 eV deeper than that of Bi^{3+}. A TL glow peak with a higher temperature is then to be expected by using the Eu^{3+} as a ~ 1.1 eV deep electron trapping centre and the Tb^{3+} and Pr^{3+} as the hole trapping centres.

Compared with Ln^{3+} single doped $LiTaO_3$ as shown in Fig. 3(c1) and (c3), a new and common TL glow peak at ~ 347 K appears in $LiTaO_3$:0.005Pr^{3+},0.001Eu^{3+} in Fig. 3(c2) and $LiTaO_3$:0.005Tb^{3+},0.001Eu^{3+} in Fig. 3(c4). The trap depth of the TL glow peak at ~ 347 K in Fig. 3(c2) and (c4) was roughly estimated to be ~ 0.81 eV by using a variable heating rate plot method (Fig. 4(d)). The determined Eu^{3+} electron trap depth (~0.81 eV) is about 0.3 eV lower than that of the predicted Eu^{3+} electron trapping depth (~1.1 eV) from the VRBE diagram in Fig. 1(a). Herein, the 347 K TL glow peak was analyzed by assuming a first-order TL-recombination kinetics and that there was no trap depth distribution in $LiTaO_3$:0.005Tb^{3+},0.001Eu^{3+}. Such a situation is not realistic in a real phosphor compound and the reported trapping depth energy (~0.81 eV) and the frequency factors of $s = 2.50 \times 10^{10}\ s^{-1}$ should be treated as indicative.

To better unravel the nature of the Eu^{3+} electron trap in $LiTaO_3$, a TL glow peak cleaning method was utilized for

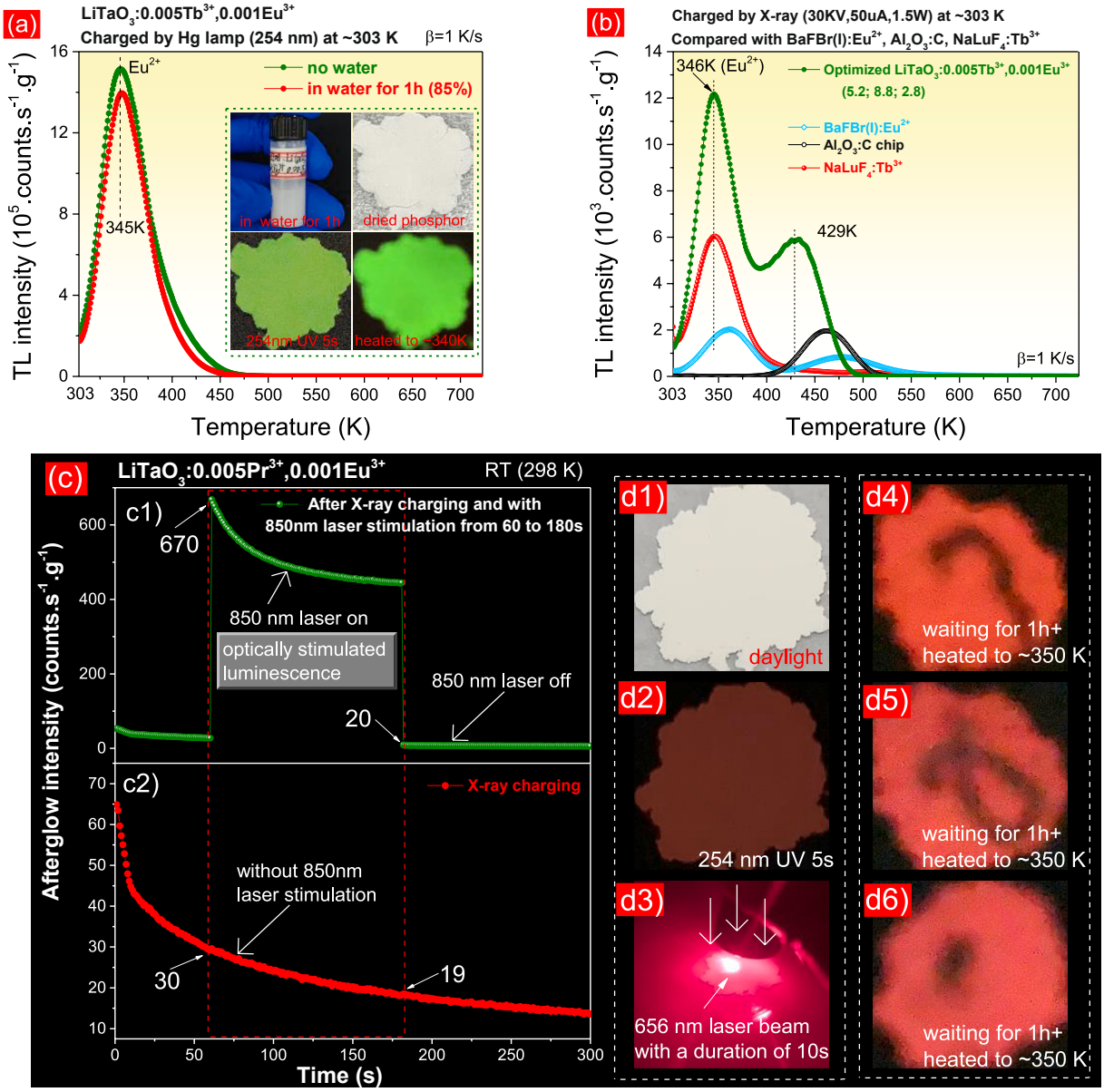

Fig. 9. (a) TL glow curve of $LiTaO_3$:0.005Tb^{3+},0.001Eu^{3+} after exposure to water for 1 h and then followed by 254 nm UV-light charging. (b) TL glow curves for the optimized $LiTaO_3$:0.005Tb^{3+}, 0.001Eu^{3+} charged by X-rays. (c) RT isothermal decay curves of $LiTaO_3$:0.005Pr^{3+},0.001Eu^{3+} after X-ray charging and with 850 nm infrared laser stimulation from 60 to 180 s. (d1) until (d6) Information display of "7", "0", and "a point" by liberating the stored charge carriers by 656 nm laser stimulation and using the thermally stimulated Pr^{3+} 4f → 4f emissions at ~350 K.

$LiTaO_3$:0.005Tb^{3+},0.001Eu^{3+}. As shown in Fig. 6, with increasing T_{clean} from 313 to 373 K, the TL glow peak gradually shifts from 346 to 401 K and the TL also gradually decreases, indicating that there is a trap depth distribution. It means that the charge carriers stored in less deep traps are liberated at T_{clean} and the charge carriers stored in deep traps still remain[58,59]. The Eu^{3+} electron trapping depth has then been determined to be in the range from ~0.82 to ~0.95 eV by the initial rise analysis plots (Fig. S16). Considering the error margins of trap depths determined by a thermoluminescence study or by a VRBE diagram prediction[27,28], the experimentally derived Eu^{3+} electron trapping depth is consistent with that (~1.1 eV) predicted by the VRBE diagram in Fig. 1(a). We therefore assign the 347 K TL glow peak in Fig. 3(c2) and (c4) to electron liberation from Eu^{2+} and recombination with holes trapped at Pr^{4+} or Tb^{4+} to generate characteristic Pr^{3+} or Tb^{3+} 4f → 4f emissions during thermoluminescence readout.

Based on the above discussion, charge carriers trapping and release processes are demonstrated in the VRBE diagram in Fig. 1(a). During X-ray exposure, free electrons and holes are created. The free holes migrate in the valence band to be captured by Pr^{3+} or Tb^{3+} to form Pr^{4+} or Tb^{4+} (arrows 1 and 2). The free electrons are captured by Eu^{3+} or Bi^{3+} to form Eu^{2+} or Bi^{2+} (arrows 3 and 5). Since the trap depths of the Bi^{3+} and Eu^{3+} electron trapping centres are less deep than that of Pr^{3+} and Tb^{3+} hole trapping centres in $LiTaO_3$, less activation energy is required to liberate the electrons stored at Bi^{2+} and Eu^{2+}. The electrons captured at Bi^{2+} or Eu^{2+} will be liberated at a lower temperature at about 283 K or 347 K (arrows 6 and 4) to recombine with the holes trapped at Pr^{4+} or Tb^{4+}, yielding typical Pr^{3+} or Tb^{3+} 4f → 4f emissions during TL-readout.

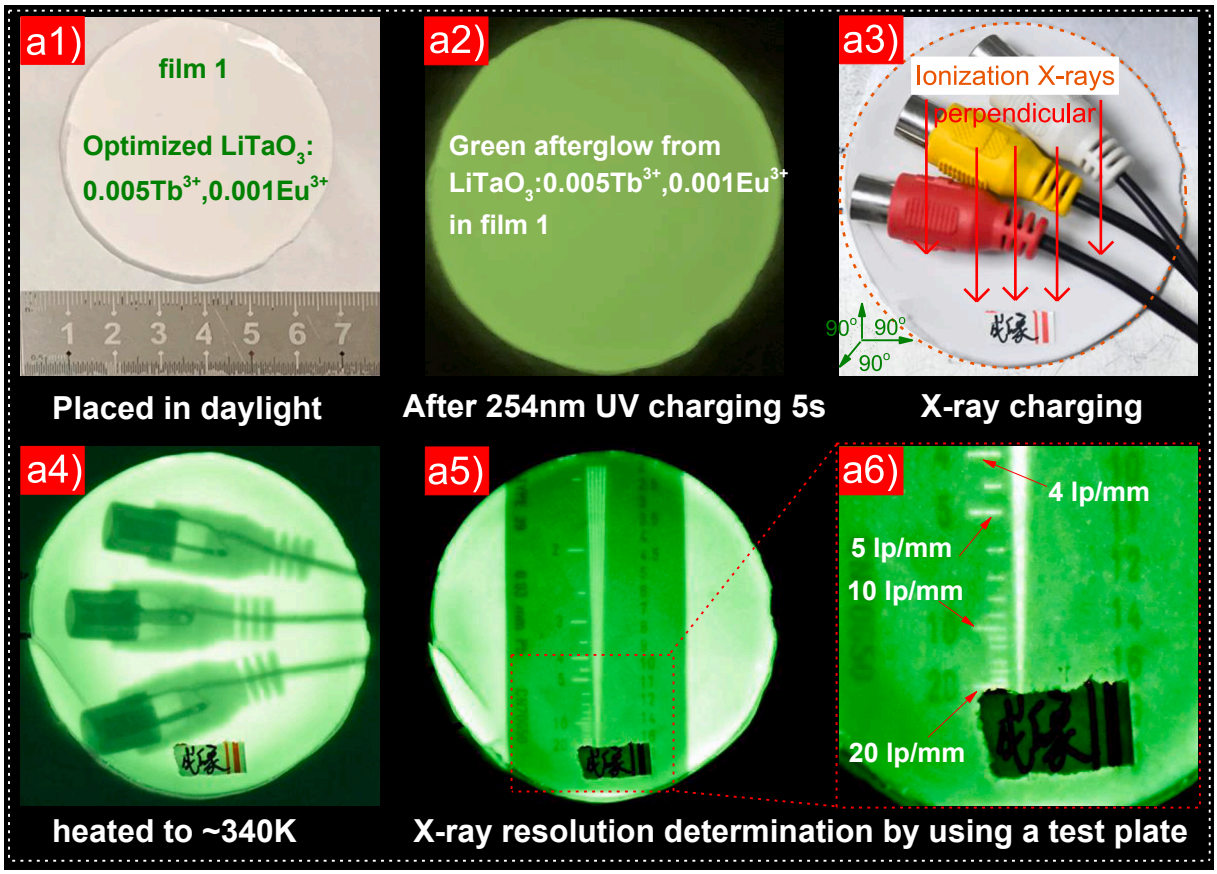

Fig. 10. Proof-of-concept plane X-ray imaging by using the optimized $LiTaO_3$:0.005Tb^{3+}, 0.001Eu^{3+}-based silicone gel film 1. (a1) and (a2) Uniform afterglow from the 254 nm UV-light charged film 1. (a3) and (a4) An X-ray imaging photograph for a large electronic connector. (a5) and (a6) X-ray imaging resolution determination by using a standard Pb-based test plate.

5. Exploring multimode applications

5.1. Exploring anti-counterfeiting application by using Eu^{3+} as a deep electron trap and the developed $LiTaO_3$:Ln^{3+},Eu^{3+} (Ln = Tb or Pr) storage phosphors

To explore anti-counterfeiting application, the synthesized $LiTaO_3$:0.005Ln^{3+},0.001Eu^{3+} (Ln = Tb or Pr) storage phosphors were further studied. Fig. 7 and Fig. S17 show the TL glow curves of $LiTaO_3$:0.005Tb^{3+},0.001Eu^{3+} charged by X-rays or 254 nm UV-light with different duration. As shown in the inset in Fig. 7, the integrated TL intensity can be fitted by $TL = 812905 \times t\text{-}1.09 \times 10^7$ ($R^2 = 0.9997$), where t means the X-ray exposure time. The similar applied to $LiTaO_3$:0.005Pr^{3+},0.001Eu^{3+} (Fig. S18). It means that $LiTaO_3$:0.005Tb^{3+},0.001Eu^{3+} and $LiTaO_3$:0.005Pr^{3+},0.001Eu^{3+} storage phosphors have potential utilization as dosimeters for X-ray detection.

Fig. 8(a)-(b) and S19(a)-19(b) show the TL glow curves of $LiTaO_3$:0.005Tb^{3+},0.001Eu^{3+} first charged by 254 nm UV-light and then followed by different energy photon stimulation. The ratios of the integrated TL glow intensity from 303 to 623 K with additional optical stimulation to that of with no additional stimulation are provided as percentage values in the legends of Fig. 8(a)-(b) and S19(a)-19(b). After 1 s or 25 s WLED stimulation (52 mW/cm^2), about 42 % or 90 % of the stored charge carriers in $LiTaO_3$:0.005Tb^{3+},0.001Eu^{3+} in Fig. 8(b) has been released, respectively.

Fig. 8(c1) shows the RT isothermal decay curve of $LiTaO_3$:0.005Tb^{3+},0.001Eu^{3+} after X-ray charging and then with 850 nm infrared laser stimulation from 60 s until 180 s in the dark. Compared with that with no 850 nm laser stimulation in Fig. 8(c2), about 8.5 times stronger 850 nm optically stimulated initial Tb^{3+} $^5D_4 \rightarrow {}^7F_j$ (j = 0–6) emissions appear in Fig. 8(c1) when the 850 nm infrared light is switched on.

Fig. 8(a) shows that 10 s 656 nm red laser stimulation liberates about 27 % of stored charge carriers in $LiTaO_3$:0.005Tb^{3+},0.001Eu^{3+}. Weak afterglow is to be expected in the phosphor area stimulated by the 656 nm red laser. This property has been exploited to show the text of "I", "L", and "Y" in the dark as demonstrated in Fig. 8(d1) until (d5) by combining with the afterglow from the 254 nm UV-light charged $LiTaO_3$:0.005Tb^{3+},0.001Eu^{3+} based film. Fig. 8(d6) shows the afterglow text of "I" together with an array of relatively intense green points. There is a light detection and ranging system (LiDAR) in an iPhone 12Pro, which can emit 905 nm infrared laser photons. The display of the array is then realized by the 905 nm infrared laser stimulated Tb^{3+} $^5D_4 \rightarrow {}^7F_j$ emissions from $LiTaO_3$:0.005Tb^{3+},0.001Eu^{3+}.

The chemical stability of a storage phosphor is important for application. As shown in the inset of Fig. 9(a), the synthesized $LiTaO_3$:0.005Tb^{3+},0.001Eu^{3+} was exposed to water for 1 h. Fig. 9(a) shows the TL glow curves of $LiTaO_3$:0.005Tb^{3+},0.001Eu^{3+} without and with exposure to water. The integrated TL intensity remains about 85 % after exposure to water with a duration of 1 h, indicating a good chemical stability of $LiTaO_3$:0.005Tb^{3+},0.001Eu^{3+}.

High charge carrier storage capacity is also important for application. Fig. 9(b) shows the TL glow curve of the optimized $LiTaO_3$:0.005Tb^{3+},0.001Eu^{3+} after X-ray charging. The ratios (r1; r2; r3) of the integrated TL intensity of the optimized $LiTaO_3$:0.005Tb^{3+},0.001Eu^{3+} to that of the state-of-the-art BaFBr(I):Eu^{2+} (r1), Al_2O_3:C chip (r2), or $NaLuF_4$:Tb^{3+} (r3), respectively, are given in the legend of Fig. 9(b).

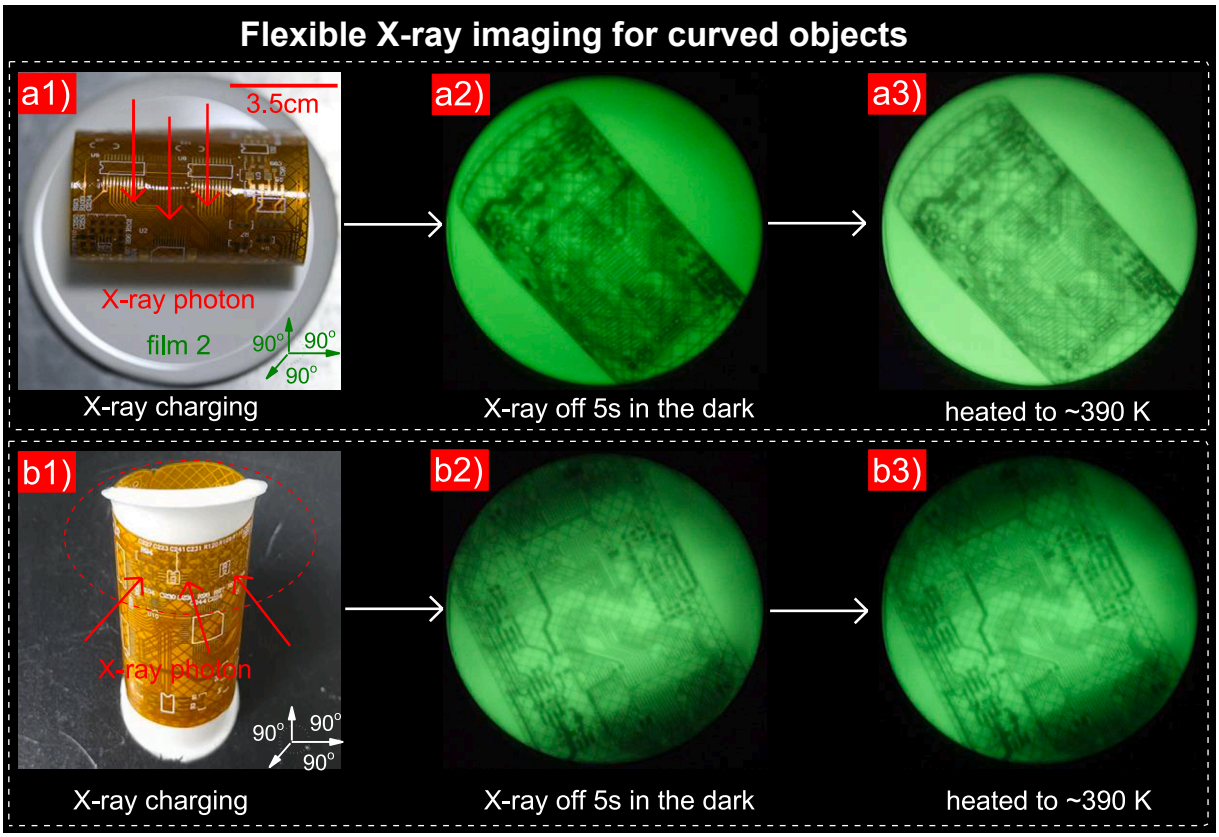

Fig. 11. Proof-of-concept flexible X-ray imaging by employing the optimized $LiTaO_3$:0.005Tb^{3+}, 0.001Eu^{3+} based flexible silicone gel film 2. (a1) until (a3) Demonstration of conventional X-ray imaging for a bended double-faced circuit board by using film 2 as a dosimeter. (b1) until (b3) Demonstration of flexible X-ray imaging by placing the bended film 2 underneath the bended circuit board.

Colour-tailorable afterglow from green to red for anti-counterfeiting application was exploited in $LiTaO_3$:0.005Pr^{3+},0.001Eu^{3+} where Eu^{3+} acts as an electron trapping centre, while Pr^{3+} acts as the hole capturing and recombination centre. Compared with that with no 656 nm stimulation in Fig. 9(c2), about 22 times stronger initial Pr^{3+} 4f → 4f emissions emerge when the 850 nm laser is switched on in Fig. 9(c1). Similar to that in Fig. 8(a) and (b), the stored charge carriers in deep traps in $LiTaO_3$:0.005Pr^{3+},0.001Eu^{3+} are liberated during the optical stimulation and weaker thermoluminescence glow intensity is then to be expected in the phosphor area with optical stimulation. Fig. 9(d3) demonstrates that the phosphor film was stimulated by 656 nm laser with different logos. After stimulation, the phosphor film was stored in the dark for 1 h. The stored information of "7", "0", and "a point" in the phosphor film is not visible during daylight, but is visible when the film was then kept at about 350 K in the dark as shown in Fig. 9(d4) until (d6) because of the thermally stimulated Pr^{3+} 4f → 4f emissions from the phosphor area where the charge carrier stored in deep traps were not liberated by 656 nm laser stimulation.

5.2. *Exploring flexible X-ray imaging by using Eu^{3+} as a deep electron trap and the optimized $LiTaO_3$:0.005Tb^{3+}, 0.001Eu^{3+} storage phosphor*

The optimized $LiTaO_3$:0.005Tb^{3+},0.001Eu^{3+} storage phosphor was dispersed in silicone gel to synthesize a flexible X-ray imaging film 1 as shown in Fig. 10(a1). The surface of the film 1 was smooth. After 254 nm UV-light charging, a uniform green afterglow film is visible in the dark as shown in Fig. 10(a2) because of the thermally stimulated Tb^{3+} $^5D_4 \rightarrow {}^7F_j$ (j = 0–6) emissions at RT. High resolution X-ray imaging photographs for a large electronic connector in Fig. 10(a3) and 10(a4), and for other objects in Fig. S21(d1) until (e5) can be obtained by using the X-ray charged film 1. A high X-ray imaging resolution of about 20 line pairs/mm (lp/mm) was realized as demonstrated in Fig. 10(a5) and (a6).

Fig. 11(a1) shows a bended double-faced circuit board. The film 2 was placed underneath the bottom of the double-faced circuit board which was horizontally exposed to X-rays. Two X-ray imaging photographs were obtained because of the thermally stimulated Tb^{3+} $^5D_4 \rightarrow {}^7F_j$ emissions from the optimized $LiTaO_3$:0.005Tb^{3+},0.001Eu^{3+} at RT in Fig. 11(a2) and at about 390 K in Fig. 11(a3). Fig. 11(a2) and (a3) show that the information of both the sides of the bended circuit board stored in the film 2 is overlapped, demonstrating the difficulty in imaging of bended objects by using traditional panel X-ray detector or dosimeter. To solve this issue, the durability and flexibility of the optimized $LiTaO_3$:0.005Tb^{3+},0.001Eu^{3+} based silicone gel X-ray imaging film 2 was utilized. Fig. 11(b1) shows that the film 2 can be well bended which can be well placed inside and underneath the bended end-to-end circuit board. After X-ray exposure, the information of the bended circuit board can be read-out by the X-ray imaging photographs as demonstrated in Fig. 11(b2) and (b3).

5.3. *Discussion: Multimode anti-counterfeiting and flexible X-ray imaging application exploration*

Colour-tailorable photoluminescence, afterglow, and thermally stimulated luminescence are explored for multimode anti-counterfeiting application. As shown in the photographs upon 254 nm UV-light illumination in Fig. 4(a2) until Fig. 4(a6), the photoluminescence colour can be tailored from green to red by increasing the doped Eu^{3+} concentration in $LiTaO_3$:0.005Tb^{3+},xEu^{3+} (x = 0.0005 until 0.006). This is because that more Eu^{3+} can give more intense characteristic red Eu^{3+} 4f

→ 4f emissions via the VB → Eu^{3+} charge transfer (CT) excitation (Fig. S8). Compared with $LiTaO_3$:0.005Tb^{3+},0.0005Eu^{3+}, about 3.5 times stronger VB → Eu^{3+} CT excitation appears in $LiTaO_3$:0.005Tb^{3+},0.006Eu^{3+} (Fig. S9). For the afterglow photographs as shown in Fig. 4(a7) until Fig. 4(a11) after 254 nm UV-light charging, green afterglow appears in the dark. This is because that Tb^{3+} acts as the main thermally stimulated recombination centre and that the role of Eu^{3+} is to mainly act as an electron trapping centre in $LiTaO_3$:0.005Tb^{3+},xEu^{3+} as evidenced in Fig. 3, Fig. 4(a1), and Fig. 4(b).

Fig. 1(b), Fig. 10, and Fig. 11 demonstrate how to realize X-ray imaging of a curved object by utilizing the flexibility and the high storage capacity of the charge carriers of the optimized $LiTaO_3$:0.005Tb^{3+},0.001Eu^{3+} based flexible silicone gel film. Fig. 4(e) shows that the integrated TL intensity of $LiTaO_3$:0.005Tb^{3+},0.001Eu^{3+} remains 93 %, 71 %, and 32 % after 60 s, 1000 s, or 1000 h, respectively. It means that the charge carriers can be stably stored in the $LiTaO_3$:0.005Tb^{3+}, 0.001Eu^{3+}. Fig. 7 and Fig. S18 shows that the integrated TL intensity linearly increases with increasing the X-ray exposure time, indicating the potential use of the $LiTaO_3$:0.005Ln^{3+},0.001Eu^{3+} (Ln = Tb or Pr) as dosimeters for X-ray detection. Fig. 9(a) shows that the TL intensity remains about 85 % after exposure to water for 1 h, implying that the $LiTaO_3$:0.005Tb^{3+},0.001Eu^{3+} is chemically stable. The ratios (r1; r2; r3) of the integrated TL intensity of the optimized $LiTaO_3$:0.005Tb^{3+},0.001Eu^{3+} to that of the state-of-the-art (r1) BaFBr(I):Eu^{2+}, (r2) Al_2O_3:C, or (r3) $NaLuF_4$:Tb^{3+} are 5.2, 8.8, or 2.8, respectively, as shown in Fig. 9(b). It means that the optimized $LiTaO_3$:0.005Tb^{3+},0.001Eu^{3+} has excellent charge carrier storage capacity. Different than $NaLuF_4$:Tb^{3+} in ref. [14], the stored charge carriers in $LiTaO_3$:0.005Ln^{3+},0.001Eu^{3+} (Ln = Tb or Pr) can be efficiently liberated by a wide range energy photon stimulation from 365 nm UV-light to 850 nm infrared light as evidenced in Fig. 8. It means that X-ray imaging of a curved object is then to be expected by optically stimulated luminescence instead of by thermal stimulation of stored charge carriers in a storage phosphor based X-ray imaging plate [24,60–62].

6. Conclusions

In this work, novel $LiTaO_3$:Ln^{3+},Eu^{3+} (Ln = Tb or Pr) storage phosphors are reported for multimode anti-counterfeiting and flexible X-ray imaging applications by combining the vacuum referred binding energy (VRBE) diagram of $LiTaO_3$ and the optimization of dopant's concentration and compound synthesis condition. Based on the prediction by the VRBE diagram of $LiTaO_3$ in Fig. 1(a), compared with Bi^{3+}, Eu^{3+} has been selected as a ~0.5 eV deeper electron capturing centre for more stable electron storage at room temperature. By combining Eu^{3+} with Ln^{3+} (Ln = Tb or Pr), new $LiTaO_3$:0.005Ln^{3+},0.001Eu^{3+} storage phosphors were developed. Herein, Eu^{3+} appears to act as a less deep electron trapping centre, while Tb^{3+} and Pr^{3+} act as deep hole trapping and recombination centres in $LiTaO_3$. During TL-readout at ~ 347 K, the electrons stored at Eu^{2+} are liberated to recombine with the holes trapped at Tb^{4+} or Pr^{4+}, yielding characteristic Tb^{3+} or Pr^{3+} 4f → 4f emissions. The charge carrier storage capacity in $LiTaO_3$:0.005Tb^{3+}, xEu^{3+} can be optimized by changing Eu^{3+} concentration and compound synthesis temperature. The ratios named as (r1; r2; r3) of the integrated TL intensity of the optimized $LiTaO_3$:0.005Tb^{3+},0.001Eu^{3+} to that of the state-of-the-art (r1) BaFBr(I):Eu^{2+}, (r2) Al_2O_3:C, or (r3) $NaLuF_4$:Tb^{3+} are 5.2, 8.8, or 2.8, respectively. More than 40 h Tb^{3+} 4f → 4f afterglow can be measurable in the $LiTaO_3$:0.005Tb^{3+},0.001Eu^{3+} charged by X-rays. The charge carriers can be stored more than 1000 h in $LiTaO_3$:0.005Tb^{3+},0.001Eu^{3+}. The charge carriers stored in $LiTaO_3$:0.005Tb^{3+},0.001Eu^{3+} can be released by a wide range energy photon stimulation from 365 nm UV-light (3.4 eV) to 905 nm infrared light (1.4 eV). Proof-of-concept anti-counterfeiting application was demonstrated by combining the colour-tailorable photoluminescence, afterglow, thermally, or optically stimulated luminescence in $LiTaO_3$:0.005Tb^{3+},xEu^{3+} and $LiTaO_3$:0.005Pr^{3+},0.001Eu^{3+}. $LiTaO_3$:0.005Tb^{3+},0.001Eu^{3+} has a high absolute scintillation light yield of 19000 ± 1800 ph/MeV. The above optical features are helpful for developing advanced multimode anti-counterfeiting applications. Proof-of-concept flexible X-ray imaging application was demonstrated by using the optimized $LiTaO_3$:0.005Tb^{3+},0.001Eu^{3+} based silicone gel film. This work not only reports promising $LiTaO_3$:0.005Ln^{3+},0.001Eu^{3+} (Ln = Tb or Pr) perovskite storage phosphors with excellent charge carrier storage capacity and stability, but also deep our understanding of trap level locations and on the trapping and liberation processes of charge carriers in inorganic compounds.

Declaration of Competing Interest

The authors declare that they have no known competing financial interests or personal relationships that could have appeared to influence the work reported in this paper.

Data availability

The data that has been used is confidential.

Acknowledgements

Dr. T. Lyu acknowledges the financial supports from the National Natural Science Foundation of China (Grant No. 12104170), the Fundamental Research Funds for the Central Universities (Grant No. ZQN-1023), the Scientific Research Funds of Huaqiao University (Grant No. 21BS106), and partly from the Instrumental Analysis Center of Huaqiao University. Dr. T. Lyu acknowledges Prof. Qiushui Chen from Fuzhou University for his assistance in X-ray imaging measurement.

Appendix A. Supplementary data

Supplementary data to this article can be found online at https://doi.org/10.1016/j.cej.2023.141685.

References

[1] W. Wei, Y. Zhang, Q. Xu, H. Wei, Y. Fang, Q. Wang, Y. Deng, T. Li, A. Gruverman, L. Cao, J. Huang, Monolithic integration of hybrid perovskite single crystals with heterogenous substrate for highly sensitive X-ray imaging, Nat. Photonics 11 (5) (2017) 315–321, https://doi.org/10.1038/nphoton.2017.43.
[2] A. Jana, S. Cho, S.A. Patil, A. Meena, Y. Jo, V.G. Sree, Y. Park, H. Kim, H. Im, R. A. Taylor, Perovskite: scintillators, direct detectors, and X-ray imagers, Mater. Today 55 (2022) 110–136, https://doi.org/10.1016/j.mattod.2022.04.009.
[3] H. Zhang, Z. Yang, M. Zhou, L. Zhao, T. Jiang, H. Yang, X. Yu, J. Qiu, Y. Yang, X. Xu, Reproducible X-ray imaging with a perovskite nanocrystal scintillator embedded in a transparent amorphous network structure, Adv. Mater. 33 (40) (2021) 2102529, https://doi.org/10.1002/adma.202102529.
[4] H. Wei, J. Huang, Halide lead perovskites for ionizing radiation detection, Nat. Commun. 10 (1) (2019) 1066, https://doi.org/10.1038/s41467-019-08981-w.
[5] W. Zhu, W. Ma, Y. Su, Z. Chen, X. Chen, Y. Ma, L. Bai, W. Xiao, T. Liu, H. Zhu, X. Liu, H. Liu, X. Liu, Y. Yang, Low-dose real-time X-ray imaging with nontoxic double perovskite scintillators, Light Sci. Appl. 9 (1) (2020) 112, https://doi.org/10.1038/s41377-020-00353-0.
[6] Z. Yang, J. Hu, D. Van der Heggen, A. Feng, H. Hu, H. Vrielinck, P.F. Smet, D. Poelman, Realizing simultaneous X-Ray imaging and dosimetry using phosphor-based detectors with high memory stability and convenient readout process, Adv. Funct. Mater. 32 (31) (2022) 2201684, https://doi.org/10.1002/adfm.202201684.
[7] W. Chen, M. Zhou, Y. Liu, X. Yu, C. Pi, Z. Yang, H. Zhang, Z. Liu, T. Wang, J. Qiu, S. F. Yu, Y. Yang, X. Xu, All-inorganic perovskite polymer-ceramics for flexible and refreshable X-Ray imaging, Adv. Funct. Mater. 32 (2) (2022) 2107424, https://doi.org/10.1002/adfm.202107424.
[8] Y.C. Kim, K.H. Kim, D.-Y. Son, D.-N. Jeong, J.-Y. Seo, Y.S. Choi, I.T. Han, S.Y. Lee, N.-G. Park, Printable organometallic perovskite enables large-area, low-dose X-ray imaging, Nature 550 (7674) (2017) 87–91, https://doi.org/10.1038/nature24032.
[9] H. Li, Y. Zhang, M. Zhou, H. Ding, L. Zhao, T. Jiang, H.Y. Yang, F. Zhao, W. Chen, Z. Teng, J. Qiu, X. Yu, Y.M. Yang, X. Xu, A solar-blind perovskite scintillator realizing portable X-ray imaging, ACS Energy Lett. 7 (9) (2022) 2876–2883, https://doi.org/10.1021/acsenergylett.2c01440.
[10] S. Yakunin, M. Sytnyk, D. Kriegner, S. Shrestha, M. Richter, G.J. Matt, H. Azimi, C. J. Brabec, J. Stangl, M.V. Kovalenko, W. Heiss, Detection of X-ray photons by solution-processed lead halide perovskites, Nat. Photonics 9 (7) (2015) 444–449, https://doi.org/10.1038/nphoton.2015.82.

[11] P.A. Rodnyi, P. Dorenbos, C.W.E. van Eijk, Energy loss in inorganic scintillators, Physica Status Solidi (b) 187 (1) (1995) 15–29, https://doi.org/10.1002/pssb.2221870102.

[12] R.T. Williams, W.W. Wolszczak, X. Yan, D.L. Carroll, Perovskite quantum-dot-in-host for detection of ionizing radiation, ACS Nano 14 (5) (2020) 5161–5169, https://doi.org/10.1021/acsnano.0c02529.

[13] P. Ran, L. Yang, T. Jiang, X. Xu, J. Hui, Y. Su, C. Kuang, X. Liu, Y. Yang, Multispectral large-panel X-ray imaging enabled by stacked metal halide scintillators, Adv. Mater. 34 (42) (2022) 2205458, https://doi.org/10.1002/adma.202205458.

[14] X. Ou, X. Qin, B. Huang, J. Zan, Q. Wu, Z. Hong, L. Xie, H. Bian, Z. Yi, X. Chen, Y. Wu, X. Song, J. Li, Q. Chen, H. Yang, X. Liu, High-resolution X-ray luminescence extension imaging, Nature 590 (7846) (2021) 410–415, https://doi.org/10.1038/s41586-021-03251-6.

[15] X. Ou, X. Chen, X. Xu, L. Xie, X. Chen, Z. Hong, H. Bai, X. Liu, Q. Chen, L. Li, H. Yang, Recent development in X-ray imaging technology: future and challenges, Research 2021 (2021) 9892152, https://doi.org/10.34133/2021/9892152.

[16] H. Wei, Y. Fang, P. Mulligan, W. Chuirazzi, H.-H. Fang, C. Wang, B.R. Ecker, Y. Gao, M.A. Loi, L. Cao, J. Huang, Sensitive X-ray detectors made of methylammonium lead tribromide perovskite single crystals, Nat. Photonics 10 (5) (2016) 333–339, https://doi.org/10.1038/nphoton.2016.41.

[17] H. Li, J. Song, W. Pan, D. Xu, W.-A. Zhu, H. Wei, B. Yang, Sensitive and stable 2D perovskite single-crystal X-ray detectors enabled by a supramolecular anchor, Adv. Mater. 32 (40) (2020) 2003790, https://doi.org/10.1002/adma.202003790.

[18] W. Pan, H. Wu, J. Luo, Z. Deng, C. Ge, C. Chen, X. Jiang, W.-J. Yin, G. Niu, L. Zhu, L. Yin, Y. Zhou, Q. Xie, X. Ke, M. Sui, J. Tang, $Cs_2AgBiBr_6$ single-crystal X-ray detectors with a low detection limit, Nat. Photonics 11 (11) (2017) 726–732, https://doi.org/10.1038/s41566-017-0012-4.

[19] B. Yang, L. Yin, G. Niu, J.-H. Yuan, K.-H. Xue, Z. Tan, X.-S. Miao, M. Niu, X. Du, H. Song, E. Lifshitz, J. Tang, Lead-Free halide Rb_2CuBr_3 as sensitive X-Ray scintillator, Adv. Mater. 31 (44) (2019) 1904711, https://doi.org/10.1002/adma.201904711.

[20] S. Cho, S. Kim, J. Kim, Y. Jo, I. Ryu, S. Hong, J.-J. Lee, S. Cha, E.B. Nam, S.U. Lee, S. K. Noh, H. Kim, J. Kwak, H. Im, Hybridisation of perovskite nanocrystals with organic molecules for highly efficient liquid scintillators, Light Sci. Appl. 9 (1) (2020) 156, https://doi.org/10.1038/s41377-020-00391-8.

[21] M. Xia, J.-H. Yuan, G. Niu, X. Du, L. Yin, W. Pan, J. Luo, Z. Li, H. Zhao, K.-H. Xue, X. Miao, J. Tang, Unveiling the structural descriptor of $A_3B_2X_9$ perovskite derivatives toward X-Ray detectors with low detection limit and high stability, Adv. Funct. Mater. 30 (24) (2020) 1910648, https://doi.org/10.1002/adfm.201910648.

[22] S. Yakunin, D.N. Dirin, Y. Shynkarenko, V. Morad, I. Cherniukh, O. Nazarenko, D. Kreil, T. Nauser, M.V. Kovalenko, Detection of gamma photons using solution-grown single crystals of hybrid lead halide perovskites, Nat. Photonics 10 (9) (2016) 585–589, https://doi.org/10.1038/nphoton.2016.139.

[23] W. Ma, T. Jiang, Z. Yang, H. Zhang, Y. Su, Z. Chen, X. Chen, Y. Ma, W. Zhu, X. Yu, H. Zhu, J. Qiu, X. Liu, X. Xu, Y. Yang, Highly resolved and robust dynamic X-Ray imaging using perovskite glass-ceramic scintillator with reduced light scattering, Adv. Sci. 8 (15) (2021) 2003728, https://doi.org/10.1002/advs.202003728.

[24] P. Leblans, D. Vandenbroucke, P. Willems, Storage phosphors for medical imaging, Materials 4 (6) (2011) 1034, https://doi.org/10.3390/ma4061034.

[25] T. Lyu, P. Dorenbos, Towards information storage by designing both electron and hole detrapping processes in bismuth and lanthanide-doped LiRE(Si, Ge)O_4 (RE = Y, Lu) with high charge carrier storage capacity, Chem. Eng. J. 400 (2020), 124776, https://doi.org/10.1016/j.cej.2020.124776.

[26] T. Lyu, P. Dorenbos, Vacuum referred binding energies of bismuth and lanthanide levels in ARE(Si, Ge)O_4 (A=Li, Na; RE=Y, Lu); towards designing charge carrier trapping processes for energy storage, Chem. Mater. 32 (3) (2020) 1192–1209, https://doi.org/10.1021/acs.chemmater.9b04341.

[27] T. Lyu, P. Dorenbos, Designing thermally stimulated 1.06 μm Nd^{3+} emission for the second bio-imaging window demonstrated by energy transfer from Bi^{3+} in La-, Gd-, Y-, and $LuPO_4$, Chem. Eng. J. 372 (2019) 978–991, https://doi.org/10.1016/j.cej.2019.04.125.

[28] T. Lyu, P. Dorenbos, Charge carrier trapping processes in lanthanide doped $LaPO_4$, $GdPO_4$, YPO_4, and $LuPO_4$, J. Mater. Chem. C 6 (2) (2018) 369–379, https://doi.org/10.1039/c7tc05221a.

[29] T. Shi, F. Liu, J. Zhang, X. Wang, Up-conversion charging of Tb^{3+}-activated garnet phosphor, J. Mater. Chem. C (2022), https://doi.org/10.1039/d2tc03380a.

[30] D. Van der Heggen, R. Zilenaite, E. Ezerskyte, V. Fritz, K. Korthout, D. Vandenberghe, J. De Grave, J. Garrevoet, L. Vincze, D. Poelman, J.J. Joos, P. F. Smet, A. Standalone, Battery-free light dosimeter for ultraviolet to infrared light, Adv. Funct. Mater. 32 (14) (2022) 2109635, https://doi.org/10.1002/adfm.202109635.

[31] A. Dobrowolska, A.J.J. Bos, P. Dorenbos, High charge carrier storage capacity in lithium lutetium silicate doped with cerium and thulium, Physica Status Solidi (RRL) – Rapid Res. Lett. 13 (3) (2019) 1800502, https://doi.org/10.1002/pssr.201800502.

[32] A. Bedard, T.D. Davis, C. Angelopoulos, Storage phosphor plates: how durable are they as a digital dental radiographic system, J. Contemp. Dent. Pract. 5 (2) (2004) 57–69.

[33] P. Huang, Z. Wen, Y. Yu, J. Xiao, Z. Wei, T. Lyu, High charge carrier storage capacity and wide range X-rays to infrared photon sensing in $LiLuGeO_4$:Bi^{3+}, Ln^{3+} (Ln = Pr, Tb, or Dy) for anti-counterfeiting and information storage applications, Mater. Chem. Front. (2023), https://doi.org/10.1039/d2qm01098d.

[34] T. Lyu, P. Dorenbos, C. Li, S. Li, J. Xu, Z. Wei, Unraveling electron liberation from Bi^{2+} for designing Bi^{3+}-based afterglow phosphor for anti-counterfeiting and flexible X-ray imaging, Chem. Eng. J. 435 (2022), 135038, https://doi.org/10.1016/j.cej.2022.135038.

[35] J. Ueda, J. Xu, S. Takemura, T. Nakanishi, S. Miyano, H. Segawa, S. Tanabe, How many electron traps are formed in persistent phosphors? ECS J. Solid State Sci. Technol. 10 (11) (2021), 116003 https://doi.org/10.1149/2162-8777/ac2e4e.

[36] H. Luo, A.J.J. Bos, P. Dorenbos, Controlled electron-hole trapping and detrapping process in $GdAlO_3$ by valence band engineering, J. Phys. Chem. C 120 (11) (2016) 5916–5925, https://doi.org/10.1021/acs.jpcc.6b00129.

[37] H. Luo, P. Dorenbos, The dual role of Cr^{3+} in trapping holes and electrons in lanthanide co-doped $GdAlO_3$ and $LaAlO_3$, J. Mater. Chem. C 6 (18) (2018) 4977–4984, https://doi.org/10.1039/c8tc01100a.

[38] P. Dorenbos, Modeling the chemical shift of lanthanide 4f electron binding energies, Phys. Rev. B 85 (16) (2012), 165107. http://link.aps.org/doi/10.1103/PhysRevB.85.165107.

[39] R.H.P. Awater, P. Dorenbos, The Bi^{3+} 6s and 6p electron binding energies in relation to the chemical environment of inorganic compounds, J. Lumin. 184 (2017) 221–231, https://doi.org/10.1016/j.jlumin.2016.12.021.

[40] P. Dorenbos, Electronic structure of Bi-activated luminescent compounds and pure bismuth photocatalytic compounds, ECS J. Solid State Sci. Technol. 10 (8) (2021), 086002, https://doi.org/10.1149/2162-8777/ac19c6.

[41] P. Dorenbos, Charge transfer bands in optical materials and related defect level location, Opt. Mater. 69 (2017) 8–22, https://doi.org/10.1016/j.optmat.2017.03.061.

[42] K. Edalati, K. Fujiwara, S. Takechi, Q. Wang, M. Arita, M. Watanabe, X. Sauvage, T. Ishihara, Z. Horita, Improved photocatalytic hydrogen evolution on tantalate perovskites $CsTaO_3$ and $LiTaO_3$ by strain-induced vacancies, ACS Appl. Energy Mater. 3 (2) (2020) 1710–1718, https://doi.org/10.1021/acsaem.9b02197.

[43] H.B. Lee, T. Dinh Hoang, Y.S. Byeon, H. Jung, J. Moon, M.-S. Park, Surface stabilization of Ni-rich layered cathode materials via surface engineering with $LiTaO_3$ for lithium-ion batteries, ACS Appl. Mater. Interfaces 14 (2) (2022) 2731–2741, https://doi.org/10.1021/acsami.1c19443.

[44] I.P. Kaminow, J.R. Carruthers, Optical waveguiding layers in $LiNbO_3$ and $LiTaO_3$, Appl. Phys. Lett. 22 (7) (1973) 326–328, https://doi.org/10.1063/1.1654657.

[45] T. Lyu, P. Dorenbos, C. Li, Z. Wei, Wide range X-Ray to infrared photon detection and energy storage in $LiTaO_3$:Bi^{3+}, Dy^{3+} perovskite, Laser Photonics Rev. 16 (9) (2022) 2200055, https://doi.org/10.1002/lpor.202200055.

[46] T. Lyu, P. Dorenbos, P. Xiong, Z. Wei, $LiTaO_3$:Bi^{3+}, Tb^{3+}, Ga^{3+}, Ge^{4+}: a smart perovskite with high charge carrier storage capacity for X-ray imaging, stress sensing, and non-real-time recording, Adv. Funct. Mater. 32 (39) (2022) 2206024, https://doi.org/10.1002/adfm.202206024.

[47] T. Lyu, P. Dorenbos, Vacuum-referred binding energies of bismuth and lanthanide levels in $LiTaO_3$ perovskite: toward designing energy storage phosphor for anti-counterfeiting, X-ray imaging, and mechanoluminescence, Laser Photonics Rev. 16 (10) (2022) 2200304, https://doi.org/10.1002/lpor.202200304.

[48] A.J.J. Bos, R.M. van Duijvenvoorde, E. van der Kolk, W. Drozdowski, P. Dorenbos, Thermoluminescence excitation spectroscopy: a versatile technique to study persistent luminescence phosphors, J. Lumin. 131 (7) (2011) 1465–1471, https://doi.org/10.1016/j.jlumin.2011.03.033.

[49] J. Ueda, P. Dorenbos, A.J.J. Bos, A. Meijerink, S. Tanabe, Insight into the thermal quenching mechanism for $Y_3Al_5O_{12}$:Ce^{3+} through thermoluminescence excitation spectroscopy, J. Phys. Chem. C 119 (44) (2015) 25003–25008, https://doi.org/10.1021/acs.jpcc.5b08828.

[50] G. Gasparotto, S.A.M. Lima, M.R. Davolos, J.A. Varela, E. Longo, M.A. Zaghete, Luminescence properties of Eu^{3+}- and Mg^{2+}-doped $LiTaO_3$ obtained via the polymeric precursor method, J. Lumin. 128 (10) (2008) 1606–1610, https://doi.org/10.1016/j.jlumin.2008.03.005.

[51] R. Zhou, F. Ma, F. Su, Y. Ou, Z. Qi, J. Zhang, Y. Huang, P. Dorenbos, H. Liang, Site Occupancies, VUV-UV–vis photoluminescence, and X-ray radioluminescence of Eu^{2+}-Doped $RbBaPO_4$, Inorg. Chem. 59 (23) (2020) 17421–17429, https://doi.org/10.1021/acs.inorgchem.0c02714.

[52] C. Liu, Z. Qi, C.-G. Ma, P. Dorenbos, D. Hou, S. Zhang, X. Kuang, J. Zhang, H. Liang, High light yield of $Sr_8(Si_4O_{12})Cl_8$:Eu^{2+} under X-ray excitation and its temperature-dependent luminescence characteristics, Chem. Mater. 26 (12) (2014) 3709–3715, https://doi.org/10.1021/cm501055k.

[53] Y. Yang, B. Lou, Y. Ou, F. Su, C.-G. Ma, C.-K. Duan, P. Dorenbos, H. Liang, Experimental and theoretical studies of the site occupancy and luminescence of Ce^{3+} in $LiSr_4(BO_3)_3$ for potential X-ray detecting applications, Inorg. Chem. 61 (19) (2022) 7654–7662, https://doi.org/10.1021/acs.inorgchem.2c01016.

[54] C.R. Ronda, A.M. Srivastava, Scintillators, in: C. Ronda (Ed.), Luminescence, Wiley-VCH Verlag GmbH & Co. KGaA, Weinheim, Germany, 2007, pp. 105–132.

[55] W. Hoogenstraaten, Electron traps in zinc–sulphide phosphors, Philips Res. Rep 13 (1958) 515–693.

[56] A.J.J. Bos, Thermoluminescence as a research tool to investigate luminescence mechanisms, Materials 10 (12) (2017) 1357, https://doi.org/10.3390/ma10121357.

[57] Y. Fangtian, J.J.B. Adrie, S. Qiufeng, H. Shihua, D. Pieter, Electron transfer process between Ce^{3+} donor and Yb^{3+} acceptor levels in the bandgap of $Y_3Al_5O_{12}$ (YAG), J. Phys. Condens. Matter 23 (21) (2011), 215502, https://doi.org/10.1088/0953-8984/23/21/215502.

[58] J. Ueda, P. Dorenbos, A.J.J. Bos, K. Kuroishi, S. Tanabe, Control of electron transfer between Ce^{3+} and Cr^{3+} in the $Y_3Al_{5-x}Ga_xO_{12}$ host via conduction band engineering, J. Mater. Chem. C 3 (22) (2015) 5642–5651, https://doi.org/10.1039/c5tc00546a.

[59] J. Ueda, S. Miyano, S. Tanabe, Formation of deep electron traps by Yb^{3+} codoping leads to super-long persistent luminescence in Ce^{3+}-doped yttrium aluminum gallium garnet phosphors, ACS Appl. Mater. Interfaces 10 (24) (2018) 20652–20660, https://doi.org/10.1021/acsami.8b02758.

[60] H. Vrielinck, F. Loncke, J.P. Tahon, P. Leblans, P. Matthys, F. Callens, Electron nuclear double resonance study of photostimulated luminescence active centers in CsBr:Eu^{2+} medical imaging plates, Phys. Rev. B 83 (5) (2011), 054102, https://doi.org/10.1103/PhysRevB.83.054102.

[61] J. Du, S. Lyu, K. Jiang, D. Huang, J. Li, R. Van Deun, D. Poelman, H. Lin, Deep-level trap formation in Si-substituted Sr_2SnO_4:Sm^{3+} for rewritable optical information storage, Mater. Today Chem. 24 (2022), 100906, https://doi.org/10.1016/j.mtchem.2022.100906.

[62] Y. Zhuang, L. Wang, Y. Lv, T.-L. Zhou, R.-J. Xie, Optical data storage and multicolor emission readout on flexible films using deep-trap persistent luminescence materials, Adv. Funct. Mater. 28 (8) (2018) 1705769, https://doi.org/10.1002/adfm.201705769.